Coastal Research And Transportation Education
Tier 1 University Transportation Center
U.S. Department of Transportation

COLLABORATIVE: SEAHIVE® solutions to mitigate bridge scour – Phase I Scour

July 6, 2026

(1) Sonia Akter, Graduate Research Assistant, Ingram School of Engineering, Texas State University, 601 University Drive, San Marcos, TX 78666; ORCID 0000-0002-7958-6221; Email: soniaakter.ce@txstate.edu
(2) Rodolfo Castillo, Graduate Research Assistant, Ingram School of Engineering, Texas State University, 601 University Drive, San Marcos, TX 78666; ORCID 0009-0002-8260-9970; Email: rch_14@txstate.edu
(3) Salah Faroughi, Ph.D., P.E., Assistant Professor, Chemical Engineering Department, University of Utah, 50 Central Campus Drive, Salt Lake City, Utah, 84112; ORCID 0000-0002-6543-1691; Email: salah.faroughi@utah.edu
(4) Landolf Rhode-Barbarigos, Ph.D. Associate Professor, Civil and Architectural Engineering, University of Miami, 1251 Memorial Drive, Coral Gables, FL 33146; ORCID 0000-0001-7550-800X; Email: landolfrb@miami.edu
(5) Stacey Kulesza, Ph.D., P.E., Associate Professor at Texas State University, Ingram School of Engineering, 601 University Drive, San Marcos, TX 78666; ORCID 0000-0003-3283-6235; Email: sekulesza@txstate.edu

Final Research Report
Prepared for:
Coastal REsearch And Transportation Education

Technical Report Documentation Page

1. Report No.	2. Government Accession No.	3. Recipient's Catalog No.
2301-11	01895141	n/a

4. Title and Subtitle COLLABORATIVE: SEAHIVE® solutions to mitigate bridge scour – Phase I	5. Report Date 9/1/2-23 - 07/06/2026
	6. Performing Organization Code n/a
7. Author(s) (1) Sonia Akte, GRA TXST; (2) Rodolfo Castillom GRA, TXST;(3) Salah Faroughi PhD, TXST; (5) Stacey Kulesza PhD TXST,Landolf Rhode-Barbarigos, Ph.D	8. Performing Organization Report No. n/a
9. Performing Organization Name and Address Ingram School of Engineering, Texas State University 601 University Dr. San Marcos, TX 78666	10. Work Unit No. (TRAIS) n/a
	11. Contract or Grant No. 69A3552348330
12. Sponsoring Agency Name and Address Office of the Assistant Secretary for Research and Technology University Transportation Centers Program Department of Transportation Washington, DC United States 20590	13. Type of Report and Period Covered Final Report 07-06-2026
	14. Sponsoring Agency Code OST-R

15. Supplementary Notes

https://create.engineering.txst.edu/

16. Abstract

This study investigates the performance of SEAHIVE®, a modular, bio-inspired concrete structure with surface perforations, as a proactive countermeasure to mitigate local scour around bridge piers. Despite increasing frequency of extreme hydraulic events, the design approach to scour remains reactive with conventional methods such as riprap and gabion mattresses after scour initiation. This research considers an alternative where scour mitigation is proactive by integrating SEAHIVE® elements to reduce flow-induced erosion before it reaches critical levels. The efficacy of SEAHIVE® as scour mitigation was explored experimentally and computationally. Experimental flume tests were conducted on both standalone and grouped SEAHIVE® configurations to quantify scour depth and energy dissipation relative to traditional circular monopiles. High-fidelity numerical simulations were performed using the SedFOAM solver within the Open FOAM framework, applying a two-phase flow model with k-ω turbulence closure to further quantify the fluid/sediment interactions. The results demonstrate that SEAHIVE® reduces vortex strength and turbulence intensity around the pier, leading to measurable improvements in scour mitigation. Experimentally, the standalone SEAHIVE® reduced scour depth by 7%, while the grouped arrangement, placed at three pier diameters upstream, achieved a 70% reduction. Numerically, the fully perforated SEAHIVE® showed a 28% reduction in scour depth, and the zigzag-patterned design achieved a 20% reduction, relative to a non-SEAHIVE® control case. Moreover, when grouped SEAHIVE® units were three pier diameters upstream, scour depth was reduced by approximately 38% and velocity magnitudes by 25%. Analysis of bed morphology and turbulence characteristics revealed that SEAHIVE® elements promoted smoother flow transitions, suppressed horseshoe vortex formation, and redistributed sediment transport away from critical zones. The consistency between experimental and numerical results underscores the validity of using SEAHIVE® in practical applications.

17. Key Words	18. Distribution Statement
Bridge scour; SEAHIVE®; Scour mitigation; SedFOAM; Flow-structure interaction	No Restrictions

19. Security Classif.(of this report)	20. Security Classif.(of this page)	21. No. of Pages	22. Price
Unclassified	Unclassified	50	n/a

Form DOT F 1700.7 (8-72) **Reproduction of completed page authorized**

ACKNOWLEDGMENT

This study was funded by the U.S. Department of Transportation through the Coastal REsearch and Transportation Education University Transportation Center under Grant Award Number 69A3552348330. The work was conducted at Texas State University in Collaboration with the University of Miami. The authors thank Steven Nolan (FDOT) and Charles Tapp (TxDOT) for feedback as project advisors.

DISCLAIMER

ABSTRACT

This study investigates the performance of SEAHIVE®, a modular, bio-inspired concrete structure with surface perforations, as a proactive countermeasure to mitigate local scour around bridge piers. Despite increasing frequency of extreme hydraulic events, the design approach to scour remains reactive with conventional methods such as riprap and gabion mattresses after scour initiation. This research considers an alternative where scour mitigation is proactive by integrating SEAHIVE® elements to reduce flow-induced erosion before it reaches critical levels. The efficacy of SEAHIVE® as scour mitigation was explored experimentally and computationally. Experimental flume tests were conducted on both standalone and grouped SEAHIVE® configurations to quantify scour depth and energy dissipation relative to traditional circular monopiles. High-fidelity numerical simulations were performed using the SedFOAM solver within the OpenFOAM framework, applying a two-phase flow model with k-ω turbulence closure to further quantify the fluid/sediment interactions. The results demonstrate that SEAHIVE® reduces vortex strength and turbulence intensity around the pier, leading to measurable improvements in scour mitigation. Experimentally, the standalone SEAHIVE® reduced scour depth by 7%, while the grouped arrangement, placed at three pier diameters upstream, achieved a 70% reduction. Numerically, the fully perforated SEAHIVE® showed a 28% reduction in scour depth, and the zigzag-patterned design achieved a 20% reduction, relative to a non-SEAHIVE® control case. Moreover, when grouped SEAHIVE® units were three pier diameters upstream, scour depth was reduced by approximately 38% and velocity magnitudes by 25%. Analysis of bed morphology and turbulence characteristics revealed that SEAHIVE® elements promoted smoother flow transitions, suppressed horseshoe vortex formation, and redistributed sediment transport away from critical zones. The consistency between experimental and numerical results underscores the validity of using SEAHIVE® in practical applications.

Keywords: Bridge scour; SEAHIVE®; Scour mitigation; SedFOAM; Flow-structure interaction.

Table of Contents

List of Figures

List of Tables

INTRODUCTION

Bridge scour is the erosion of streambed material surrounding bridge foundations due to hydraulic forces exerted by flowing water. It remains one of the leading causes of bridge failures in the United States; Xiong et al. (2023) report that approximately 31.53% of documented bridge collapses are attributed to scour. A notable case illustrating the severity of this issue is the 1987 collapse of the Schoharie Creek Bridge in New York, where scour-induced exposure of the pier foundations led to failure and the loss of ten lives (Feld and Carper 1996). Scour phenomena are categorized into three types as shown in Figure 1: general scour, contraction scour, and local scour (Arneson et al. 2012). This research focuses on local scour at bridge piers as it poses the most immediate structural risk.

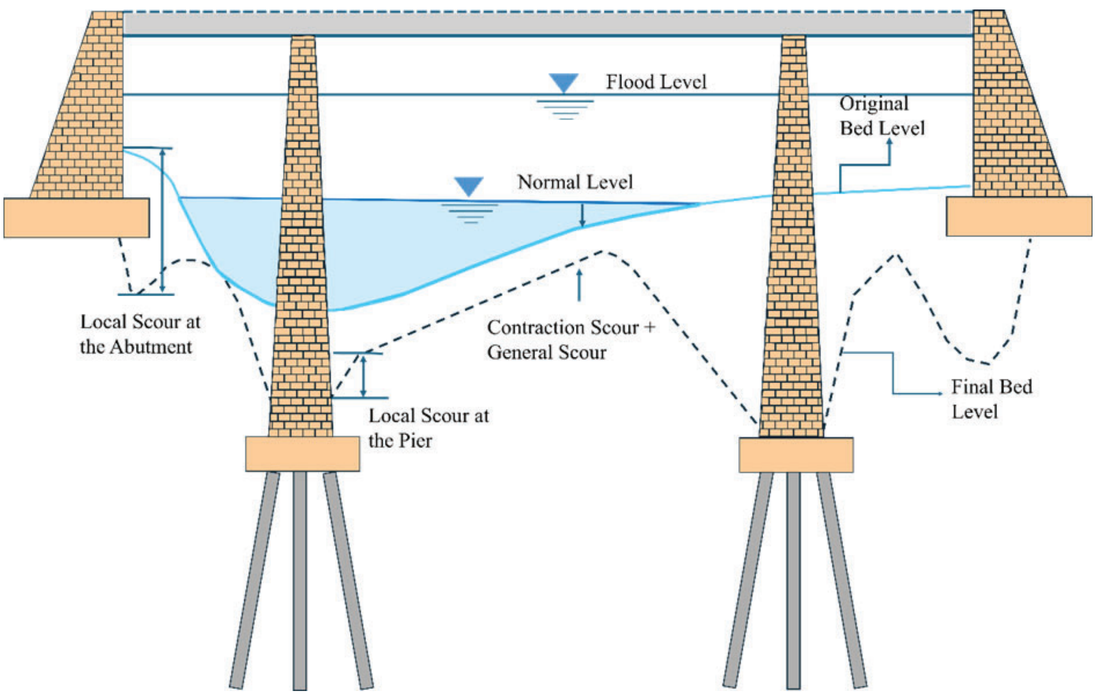

Figure 1. Three types of scour (Melville and Coleman 2000)

Local scour develops due to complex flow structures generated as water interacts with a pier. A high velocity downflow jet forms at the upstream face, impinging on the bed and initiating a horseshoe vortex system, while wake vortices develop downstream. Figure 2 illustrates the formation and structure of these vortices in the region surrounding a cylindrical pier. These vortices increase local bed shear stress, mobilize sediment, and drive the formation and growth of a scour hole until an equilibrium condition is reached (Breusers et al. 1977; Richardson and Davis 2001). The equilibrium scour depth depends on parameters such as flow intensity, pier geometry, sediment size, and flow depth (Melville and Chiew 1999). Increased frequency of extreme hydrologic events further exacerbates scour risk, particularly for aging infrastructure and bridges in flood-prone environments (Harris et al. 2019; Xiong et al. 2023). Consequently, the development of innovative and resilient countermeasures for scour mitigation has become a critical need in modern infrastructure engineering (Bharadwaj et al. 2025).

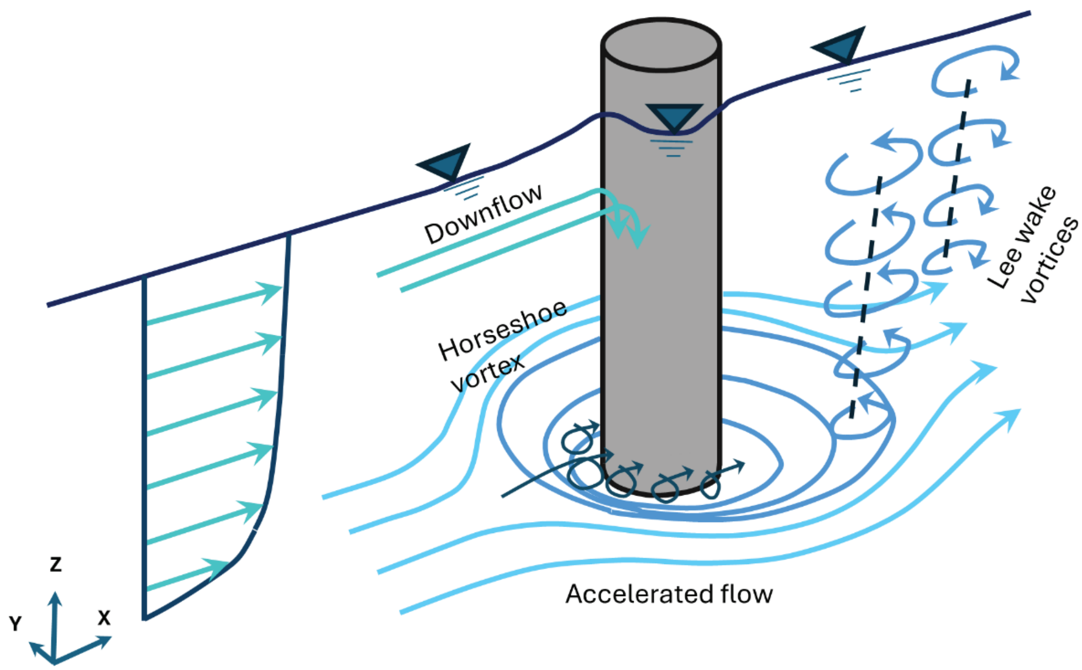

Figure 2. Schematic of flow structures and local scour holes around a cylindrical pier.

Current scour countermeasures rely largely on passive structural approaches such as riprap and gabion mattresses (Schuring et al. 2012). While widely used due to their simplicity and cost-effectiveness, these systems are susceptible to displacement, material degradation, and performance uncertainty under high-flow conditions (Singh et al. 2022; Craswell and Akib 2020). Alternative designs, including collars, slots, and flow-altering pier geometries, aim to weaken vortex formation and reduce near-bed velocities. Although laboratory studies have demonstrated reductions in scour depth exceeding 50% for certain configurations (Bestawy et al. 2020; Farooq and Ghumman 2019), these approaches are not widely implemented at field scale. These limitations highlight the need for robust countermeasures that actively modify flow structures rather than relying solely on passive resistance.

Recent advances in bio-inspired engineering have introduced innovative approaches for hydraulic stability by mimicking natural systems (Egan et al. 2015). The SEAHIVE® system shown in Figure 3 represents a modular, porous structure designed to dissipate hydraulic energy and alter near-bed flow behavior. Inspired by the shape of a beehive and density of mangrove root systems, SEAHIVE® consists of hexagonal units with vertically oriented voids that generate distributed flow resistance, reduce turbulence intensity, and disrupt coherent vortex formation. Unlike conventional armoring methods, SEAHIVE® functions as an active countermeasure by modifying the flow field, weakening downflow momentum at the pier face, and inhibiting the development of horseshoe vortices. Despite its promise, the application of SEAHIVE® as a bridge pier scour countermeasure remains underexplored. There is limited quantitative understanding of how modular, porous flow-altering systems influence near-bed hydrodynamics, turbulence structure, and equilibrium scour depth under controlled hydraulic conditions. In particular, the effectiveness of SEAHIVE® across different configurations and its interaction with sediment transport processes in fluvial environments have not been systematically evaluated.

(a) (b)

Figure 3. SEAHIVE® elements (a) hexagonal cross section (b) stacked along the coastline.

To address this knowledge gap, this study investigates the performance of SEAHIVE® installations around cylindrical bridge piers through a combined experimental and numerical approach. The initial phase evaluates a single SEAHIVE® unit as a standalone monopile in comparison to a baseline cylindrical monopile condition. This phase was conducted both experimentally and numerically. The experimental investigation focused on a standard

SEAHIVE® orientation, in which the primary face is aligned with the incoming flow to directly interact with the horseshoe vortex region. Complementary numerical simulations extended this analysis by examining variations in internal void (hole) patterns to assess their influence on flow modification. These results establish a foundational understanding of SEAHIVE®–flow interactions and serve as a basis for future development of vertically installed configurations, including skirt-type systems around bridge piers.

Building on this foundation, the second phase examines a horizontal three-unit stacked SEAHIVE® configuration placed on the sediment bed at systematic distances upstream of the pier. This configuration was evaluated through coordinated laboratory flume experiments and high-resolution numerical simulations to quantify reductions in maximum scour depth and to characterize the associated flow field, including velocity distributions, turbulence structures, and bed shear stresses. By directly linking scour outcomes with flow behavior, this phase provides insight into the mechanisms by which grouped SEAHIVE® systems influence local hydraulics. This work contributes to a broader consortium effort aimed at advancing SEAHIVE® toward field implementation, providing transportation agencies with detailed performance data and a range of deployment strategies to support site-specific design and installation decisions.

MATERIALS AND METHODOLOGY

Flume and Sediment Setup

Physical experiments were conducted in a recirculating hydraulic flume located at Texas State University (TXST). The flume is 10.0 m long, 30.0 cm wide, and 45.0 cm tall, with a downstream reservoir tank that maintains continuous flow circulation through a connected pump. Flow velocity was regulated using a flow meter adjacent to the pump. The test section consisted of a 100 cm long, 12.5 cm deep sediment bed constructed using F-65 Ottawa sand. The sand has a median grain size $d_{50} = 0.21$mm and geometric standard deviation $\sigma_g = 1.41$, satisfying the clear-water scour criterion $\sigma_g < 1.5$ (Tafarojnoruz et al. 2012). The material is classified as poorly graded sand (SP) according to the Unified Soil Classification System. The bed was prepared by air pluviation before each test to maintain consistent density. Recessed tile floors on either side stabilized the bed and a gravel ramp transitioned the flow from the upstream approach to the test section. To avoid sidewall effects influencing scour development, the flume width to pier diameter ratio (w/D) was kept greater than 6.25, as suggested by Raudkivi and Ettema (1983). For the circular monopiles, this resulted in a w/b ratio of approximately 12. Figure 4 shows the schematic of the experimental flume and key components.

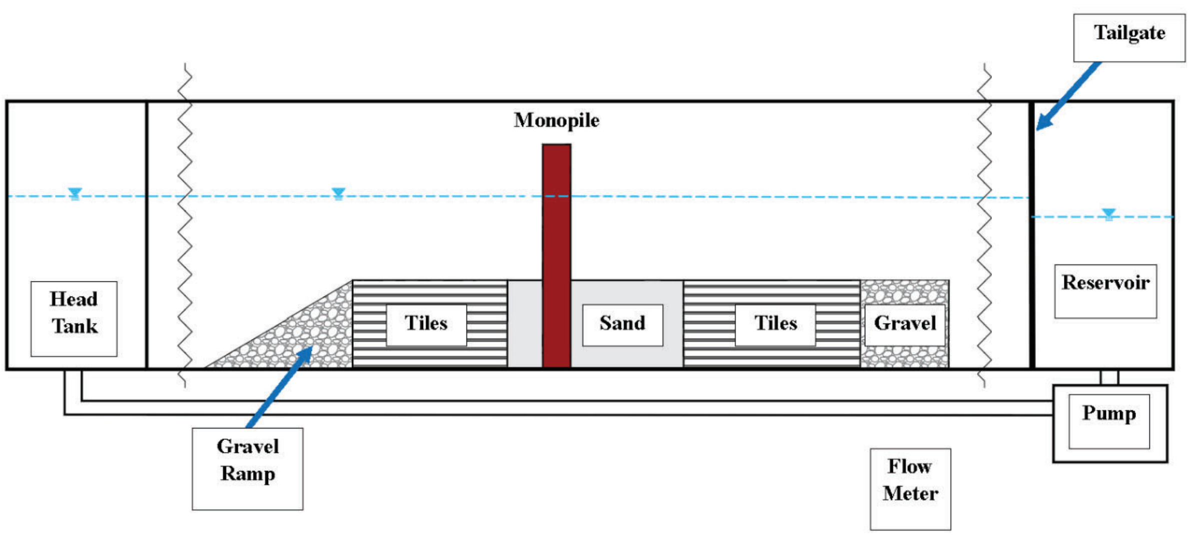

Figure 4. Experimental flume layout with monopile and sediment configuration.

Hydraulic Conditions and Clear-Water Scour

Flow depth $H$was set to 20 cm to satisfy $H/D > 3.5$, ensuring minimal influence of flow depth on scour development (Melville and Sutherland 1988). The tailgate at the downstream end of the flume-controlled water level, maintaining a Froude number, $Fr < 0.2$, and subcritical conditions (Roulund et al. 2005). The critical bed and mean velocities for the selected sediment were estimated using Melville's empirical relations (Melville 1997), and clear-water conditions were maintained by keeping the approach velocity Vin the range $0.9 < V/V_c < 1.0$.

The maximum expected scour depth under clear-water conditions was estimated using the HEC-18 equation proposed by Lagasse et al. (2012),

$$y_s = 2\ {F_r}^{0.43} D\ H^{0.35}, \tag{1}$$

where y_s is the maximum scour depth (m), F_r is the Froude number, D is the pier diameter (m), and H is the flow depth (m). According to Equation 1, the 12.5 cm bed depth was sufficient, and the scour would not reach the floor. This design ensured all measured scour depths remained less than half the bed depth.

SEAHIVE® and Monopile Configurations

Two hydrodynamically equivalent monopile geometries were used: a circular PVC monopile and a SEAHIVE monopile. In addition, a three-unit SEAHIVE group was tested in front of a circular monopile.

Single-unit configurations (Phase 1)

For Phase 1, a circular monopile and a SEAHIVE® model were tested. Both were 45 cm tall with an equivalent cross-sectional area to ensure comparable hydraulic conditions. The SEAHIVE® monopile was fabricated as a regular hexagonal prism using 6.35 mm thick steel plates. To simulate a conservative clogged, or worst-case condition, the bottom 15.75 cm of the SEAHIVE® monopile had no perforations. As shown in Figure 5, three flow configurations were used: (1) circular monopile, (2) SEAHIVE® monopile with a vertex facing the flow, and (3) SEAHIVE® monopile with an edge facing the flow. Additionally, for the edge-facing configuration, an extra case with perforated ends embedded in the sand was tested. These tests quantified baseline scour behavior and flow modification for a single SEAHIVE unit relative to a conventional monopile. Corresponding numerical simulations were carried out for the same geometries and hydraulic conditions, including sensitivity to alternative internal perforation patterns.

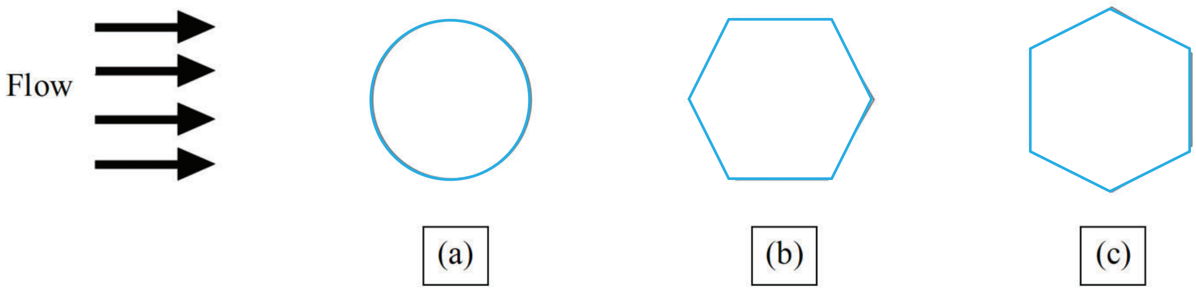

Figure 5. Monopile cross-section shapes and orientations: (a) circular, (b) SEAHIVE® face-normal, (c) SEAHIVE® vertex-normal under flow.

Three-unit SEAHIVE group (Phase 2)

In Phase 2, a three-unit SEAHIVE group was constructed by attaching three 30.0 cm long SEAHIVE units to form a horizontally stacked structure spanning the flume width. The group was placed on the sediment bed upstream of a 4.0 cm diameter circular monopile at systematic spacings of 2D, 3D, and 4D, where $D$is the monopile diameter. The physical ends of the group contacted the glass walls to provide stability and uniform exposure to the incoming flow. All other geometric, sediment, and hydraulic conditions remained unchanged from Phase 1. This configuration was designed to assess how grouped SEAHIVE units alter the approach flow, weaken downflow and horseshoe vortices, and reduce local scour depth and volume compared to the unprotected monopile.

Meaasurement and Data Processing

Scour depth at the monopile face was monitored using a tape scale fixed to the front of the pile, where the deepest scour was expected due to downflow effects. During each experiment, measurements were recorded at short intervals in the early stages and increased as scour approached equilibrium:

- Every 5 min during the first hour.
- Every 30 min thereafter until five successive measurements over approximately two hours showed no change in depth, indicating equilibrium scour.

At the end of each test, the flume was drained slowly to minimize disturbance of the bed. The final scour volume was measured using two methods: (1) manual displacement volume measurement using water-filled plastic sheeting, and (2) digital photogrammetry. The latter required capturing a short video of the bed, which was processed with the Scaniverse mobile application to create a 3D mesh. The mesh was then imported into CloudCompare for analysis. Bed contours were reconstructed at a common zero reference elevation, and scour-hole and wake-deposition volumes were extracted for each configuration. Temporal scour data were fitted with a classic exponential clear-water scour model to estimate equilibrium depth $d_{se}$and characteristic time T_e. The goodness of fit was evaluated using correlation coefficients between measured and modeled scour depth.

Numerical Framework and Validation

Numerical simulations were performed using SedFOAM, an open-source, two-phase Eulerian–Eulerian solver built on OpenFOAM, to model coupled water–sediment interactions around the control monopile and SEAHIVE® configurations. The simulations were conducted under hydraulic conditions consistent with the laboratory flume experiments to enable direct comparison between measured and predicted scour behavior. The computational domain reproduced the TXST flume geometry and consisted of a sand bed overlain by a water column, with either the control monopile or SEAHIVE® configuration centered in the test section. Inflow conditions were prescribed to match the experimental approach velocity, and a logarithmic inlet velocity profile was applied. The domain was discretized using an unstructured mesh with local refinement near the structure and the sediment–water interface to capture near-bed flow gradients and sediment transport processes. A mesh sensitivity analysis was performed using coarse, medium, and fine mesh resolutions to evaluate the effect of spatial discretization on predicted scour depth. Because the medium and fine meshes produced similar scour evolution and equilibrium scour depth, the medium-resolution mesh was selected as the best balance between computational efficiency and predictive accuracy. Detailed governing equations, constitutive closures, domain setup, boundary conditions, and mesh design are provided in Appendix A.

The numerical model was validated against both published and in-house experimental data. First, the model was compared with the monopile scour experiments of Roulund et al. (2005) to verify its ability to reproduce the time evolution of normalized scour depth. It was then compared with the TXST control-monopile experiments and selected SEAHIVE® cases used in this study. Following validation, the numerical simulations were used to interpret the hydrodynamic mechanisms associated with scour mitigation, including changes in normalized scour depth, near-bed tangential and vertical velocities, and coherent vortex structures. Definitions of the near-bed flow metrics used for vortex identification are provided in Appendix A.4. Together, the numerical and experimental results provide a consistent basis for evaluating how single-unit and grouped SEAHIVE® configurations modify local flow behavior and reduce scour potential.

Quantitative Measures of Model Agreement

Agreement between numerical and experimental scour results was evaluated using relative error (RE) and mean squared error (MSE). These metrics were computed using corresponding time-series measurements of scour depth for each validation case, including the published monopile benchmark, the TXST control monopile, and the selected SEAHIVE® configuration. The relative error at each time step was calculated as the absolute difference between simulated and experimental scour depth, normalized by the experimental value:

$$RE_i = \left| \frac{d_{s,\mathrm{num},i} - d_{s,\exp,i}}{d_{s,\exp,i}} \right| \times 100 \tag{2}$$

where $d_{s,\mathrm{num},i}$ is the simulated scour depth, $d_{s,\exp,i}$ is the corresponding experimental scour depth, and i denotes the time step. The mean squared error was calculated as

$$MSE = \frac{1}{n}\sum_{i=1}^{n}\left(d_{s,\mathrm{num},i} - d_{s,\exp,i}\right)^2 \tag{3}$$

where n is the total number of time steps included in the comparison. Relative error was used to assess point-by-point agreement over time, while MSE provided a single cumulative measure of deviation across the full scour history. These metrics were used to support the validation discussion by quantifying the ability of the numerical framework to reproduce both the temporal evolution and magnitude of scour observed experimentally.

SINGLE SEAHIVE®SYSTEM

The Single SEAHIVE® configuration was assessed to determine its effectiveness in mitigating local scour to replace a cylindrical pier under clear-water flow conditions. These results will be used to guide future work where single, vertical SEAHIVE® are placed upstream and/or around a pier as a skirt. To comprehensively evaluate its performance, both physical model testing and numerical simulations were conducted. The experimental campaign focused on quantifying scour depth evolution over time and documenting changes in bed morphology, while the numerical approach provided detailed flow field visualization and vortex structure analysis using turbulence modeling and sediment transport simulation. The analysis emphasizes direct comparison between the Single SEAHIVE® and control (no countermeasure) cases, enabling a clear understanding of the hydrodynamic benefits introduced by the SEAHIVE® unit. Specifically, the investigation aimed to (i) track the reduction in maximum scour depth, (ii) analyze changes in flow acceleration and vortex intensity, and (iii) evaluate spatial distribution of sediment deposition and erosion.

Scour Assessment for Single SEAHIVE®

The single SEAHIVE® monopile system was experimentally investigated under clear-water flow conditions to assess its potential in mitigating local scour compared to a conventional circular monopile. Figure 6 presents the temporal evolution of scour depth d_s for the circular monopile and the three SEAHIVE® monopile orientations tested under identical clear-water conditions. The circular monopile with a solid base reaches an equilibrium scour depth of approximately 3.7 cm after about 400–500 min. The scour progressed rapidly during the initial phase, with approximately 78% of the total depth forming within the first hour. The SEAHIVE® monopile with a vertex facing the flow (solid base) develops a slightly deeper equilibrium scour depth of about 4.3 cm, whereas the SEAHIVE® monopile with an edge perpendicular to the flow and a solid base reaches roughly 3.8 cm. The configuration with an edge perpendicular to the flow and a perforated base produces the largest equilibrium scour depth, approaching 4.5 cm. All SEAHIVE® configurations exhibit a rapid initial scour phase within the first 60–90 min, like the circular monopile, followed by a gradual approach to equilibrium. These results indicate that, for a single SEAHIVE® monopile installed in place of a circular monopile, changes in orientation and base perforation primarily influence the magnitude of equilibrium scour rather than the overall time scale of scour development.

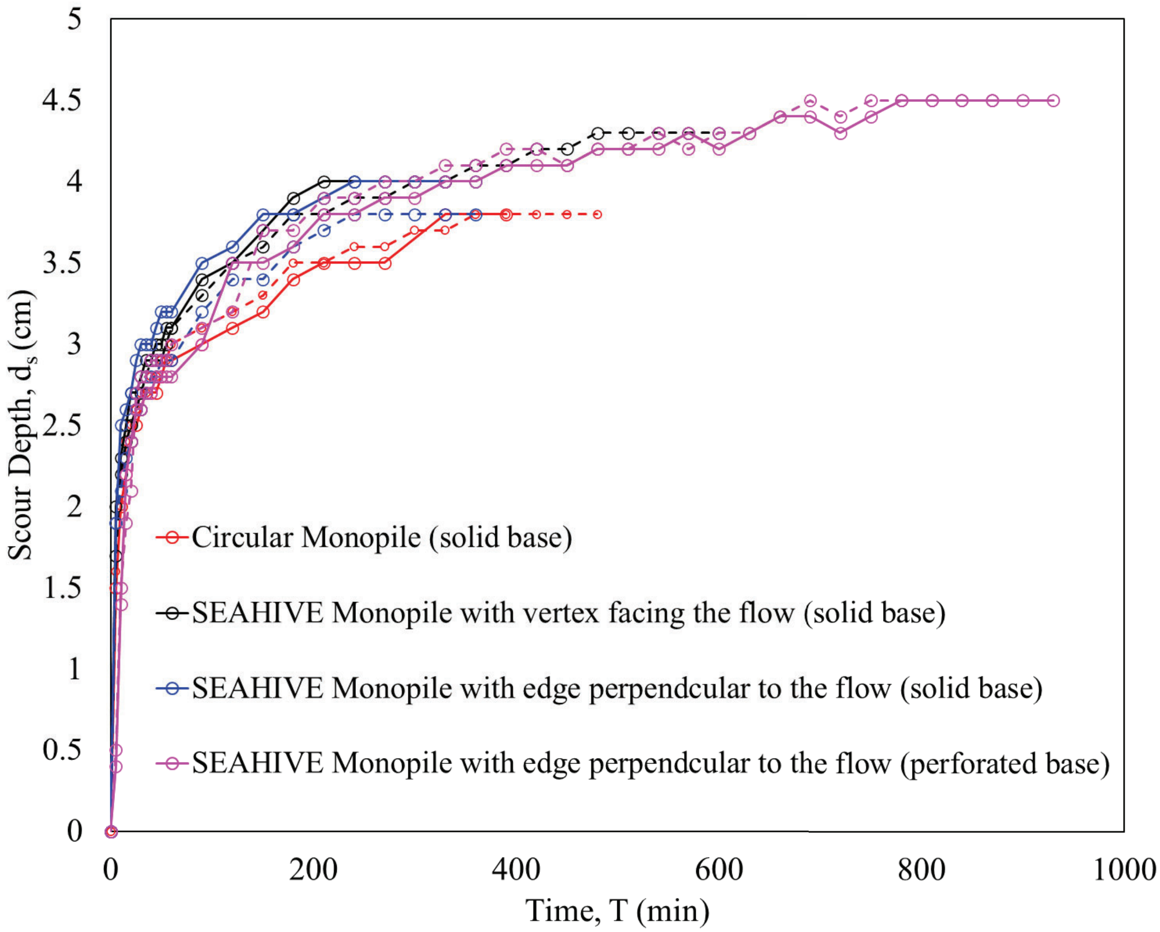

Figure 6. Scour development curves for circular monopile and SEAHIVE® configurations.

To support these observations, a volumetric image analysis was conducted which involved 3D reconstruction followed by mesh point generation to quantify sediment loss. Manual measurement of the base case produced a scour volume of 227 cm^3, while photogrammetry yielded a slightly higher value of 285 cm^3, indicating improved spatial representation from the image-based method. Key quantitative outcomes including final scour depths, volumes obtained through both manual and photogrammetric methods, and the time required to reach equilibrium for each configuration are compiled in Table 1.

Table 1. Experimental results for circular monopile compared to three SEAHIVE® configurations with replicates.

Configuration	V_m (cm^3)	V_q (cm^3)	d_s (cm)	t ($hours$)
Circular Monopile (solid base, case a)	-	-	3.8	8
	227	285	3.8	8
SEAHIVE® Monopile with vertex facing the flow (solid base, case b)	375	334	4.3	10.0
	389	334	4.3	10.0
SEAHIVE® Monopile with edge perpendicular to the flow (solid base, case c)	204	235	3.8	6.0
	200	238	3.8	6.0
SEAHIVE® Monopile with edge perpendicular to the flow (perforated base, case c)	329	340	4.5	15.5
	327	340	4.5	14.5

*V_m = manual volume measurement, V_q = volume measurement via photogrammetry, d_s = scour depth, t = time

Numerical Analysis around Single SEAHIVE®

This numerical evaluation focuses on understanding and enhancing the hydraulic performance of a single, vertically oriented SEAHIVE® monopile. Experimental results showed that a standalone SEAHIVE® monopile does not reduce scour relative to a conventional circular monopile, motivating a targeted assessment of how its internal geometry and perforation patterns influence local flow dynamics. In this phase, the SEAHIVE® design is systematically varied to explore potential performance improvements and to build a detailed understanding of the flow structures around a vertical SEAHIVE® for future skirt-type configurations. Key design features such as perforation density, alignment, and module spacing, as illustrated in Figure 7, were varied. Tested configurations include models with no perforations in the lower 15 cm, designs where perforations begin 12 cm above the base, and fully perforated units, as well as alternative zigzag perforation patterns intended to enhance near-bed energy dissipation. These numerical simulations quantify how perforation placement and pattern affect velocity reduction, vortex formation, and sediment mobilization, providing guidance for refining SEAHIVE® geometries that may be deployed as skirts or in combination with other modules in subsequent work.

.

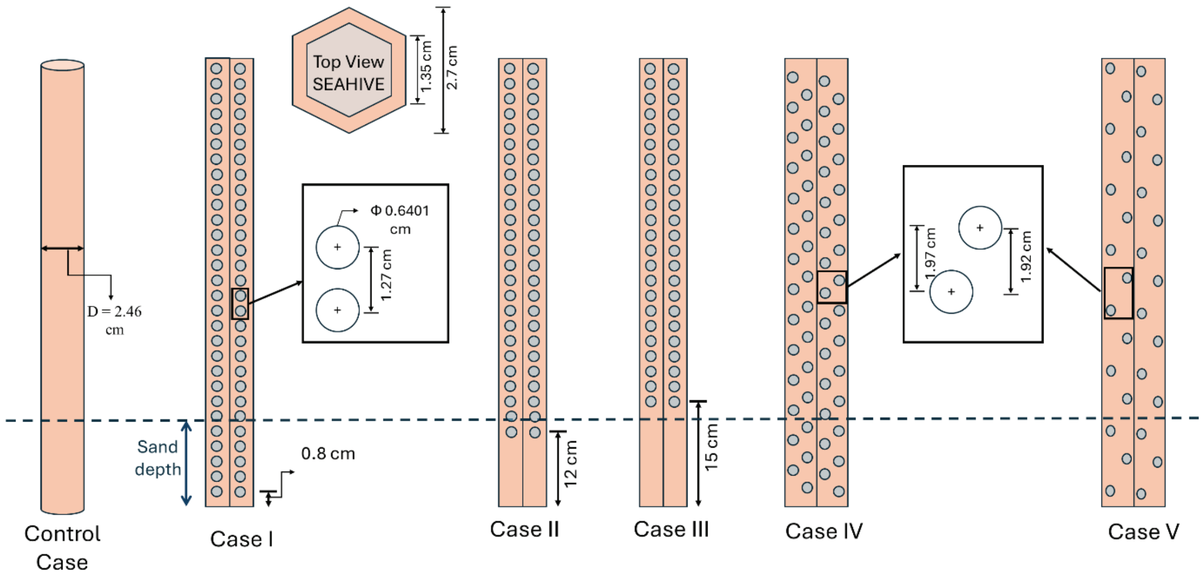

Figure 7 Schematic numerical Geometry setup of SEAHIVE®.

To evaluate how SEAHIVE® geometry influences wake development, Figure 8 shows the streamwise velocity field (Ux) for the Control Case (circular monopile with D = 2.46 cm) and SEAHIVE® Cases I–V at T = 2, 4, 6, and 8 s. In the Control Case, the flow exhibits typical vortex shedding, with strong streamlines near the monopile at the start and well-defined wake vortices forming by T = 4s. These vortices grow and extend downstream over time. In Case III, with the lower 15 cm unperforated, the flow initially resembles the Control Case, but the wake becomes less organized later. The solid lower portion restricts flow, causing higher near-bed velocity. Downstream, the wake appears weaker, suggesting some energy loss due to upper perforations. Case II, with perforations starting 12 cm from the base, allows more flow through the structure, reducing vortex strength and turbulence near the bed. This helps to diffuse the wake and may lower scour risk. In Case I, which is fully perforated, the wake is significantly diffused throughout all time steps. Coherent vortices are largely replaced by smaller, scattered eddies, reflecting strong energy dissipation within the SEAHIVE® and a substantial weakening of wake turbulence acting on the bed.

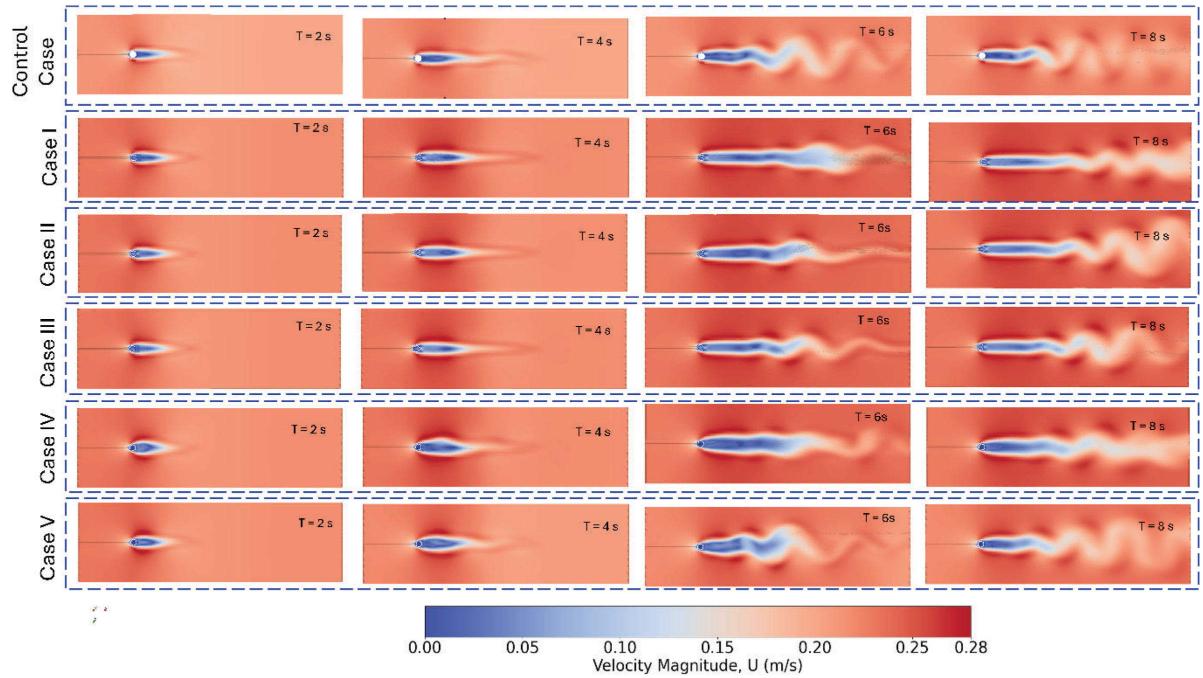

Figure 8. Temporal evolution of flow fields around Control Case and SEAHIVE® configurations.

Figure 9 shows the final scour topography around the Control Case and SEAHIVE® Cases I–V, highlighting differences in sediment erosion patterns. In the Control Case, a deep, concentrated scour region forms immediately in front of and around the sides of the monopile, with steep, closely spaced contours indicating strong localized erosion driven by the downflow and horseshoe vortex. Sediment is eroded near the pile and deposited downstream, producing elongated contours and a relatively symmetric scour pattern aligned with the wake. In Case III, where the lower 15 cm of the SEAHIVE® is unperforated, a similar central scour pit develops, but the contours are more irregular, indicating modified sediment transport paths due to the blocked lower section. Localized, enclosed contours near the base suggest intensified near-bed shear stress. In Case II, with perforations starting 12 cm above the bed, the maximum scour depth is slightly lower and more laterally dispersed than in Case III, corresponding to a 16.14% reduction in scour depth. This broader, shallower pattern is consistent with reduced turbulence concentration and more uniform sediment mobilization around the unit.

The fully perforated SEAHIVE® (Case I) exhibits the most uniform scour distribution, with smoother contour gradients and a 28.1% reduction in maximum scour depth compared with Case III. The more diffuse contours indicate that flow penetration through the unit weakens the horseshoe vortex and attenuates near-bed turbulence. Case IV shows a more structured erosion pattern with twin depressions and locally steep gradients, suggesting the presence of paired vortical structures and focused sediment removal. Case V displays a more fragmented scour footprint, with multiple irregular erosion pockets and a 20.14% reduction in depth relative to Case III. The nonuniform contours in Case V indicate complex wake interactions and spatially variable recirculation associated with its distinct perforation layout.

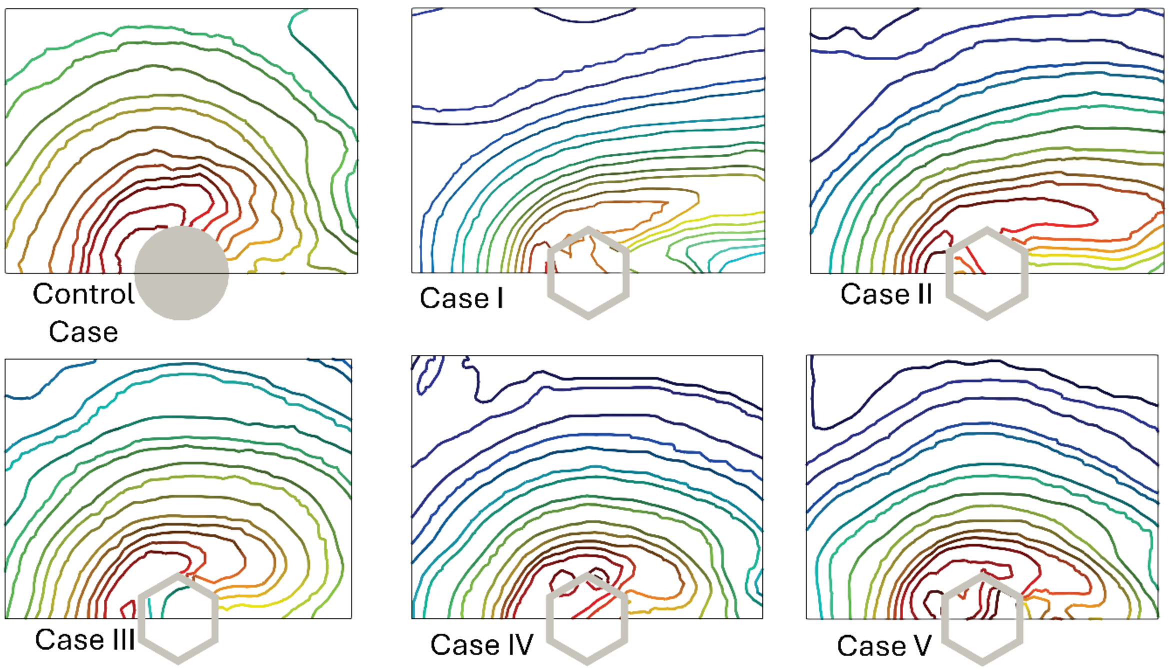

Figure 9. Bed topography for cylindrical and different SEAHIVE® configurations.

Case I not only reduces scour but also produces the smoothest and most stable wake among the single SEAHIVE® configurations. Compared with Case III, which has an unperforated lower section, Case I shows a more diffused velocity field downstream (Figure 8) and a broader, shallower scour footprint (Figure 9), indicating weaker concentration of turbulence and reduced localized erosion. Case III maintains a more compact scour pit and a sharper wake core, consistent with stronger near-bed velocities and more focused flow separation. Case V, with a zigzag perforation layout, develops a longer and more irregular wake in the velocity plots and a fragmented scour pattern with multiple localized depressions, suggesting more chaotic wake behavior and less efficient energy dissipation than Case I. The qualitative pressure response inferred from these patterns is consistent with the scour and velocity observations. The Control

Case and configurations with limited near-bed perforation (e.g., Case III) show concentrated erosion immediately in front of and around the structure, which implies stronger pressure gradients and higher near-bed shear. In contrast, the fully perforated Case I distributes scour more evenly and weakens the downstream wake, indicating that flow penetration through the unit reduces the intensity of the horseshoe vortex and mitigates peak loads on the bed. Cases IV and V, although perforated, retain more pronounced wake features and nonuniform scour zones, suggesting that their perforation layouts do not diffuse turbulence as effectively as the continuous vertical perforation in Case I.

While open perforations near the bed improve hydraulic performance in the simulations, partial clogging of the lower section is expected in field conditions. Previous studies of porous and multi-chamber coastal structures have shown that such clogging can form a sand trap that buffers flow and softens near-bed shear zones (Bergmann and Oumeraci 2012; Fugazza and Natale 1992). In the context of Case I, even if the lowest portion becomes filled with sediment, the remaining perforated height still allows flow to pass through the unit, preserving some pressure relief and wake attenuation. By contrast, configurations with fewer or higher-placed perforations have less capacity to redirect flow once the lower region is obstructed, so they are more likely to maintain strong pressure gradients and localized turbulence. Practical measures such as larger or tapered lower perforations, sacrificial liners, or filter layers could be used to manage clogging while retaining the beneficial flow-altering behavior (Schoonees et al. 2019).

Alternative perforation layouts tested in Cases IV and V, which use staggered or zigzag patterns, were intended to balance flow control and anti-scour performance. However, the velocity fields and scour contours show that these layouts produce longer, more persistent wakes and less favorable scour distributions than the fully perforated design. Overall, the numerical results indicate that continuous vertical perforation across the full height of a single SEAHIVE® unit is more effective at diffusing turbulence, attenuating the wake, and distributing scour than the other configurations examined.

Single SEAHIVE® Summary

Taken together, the experimental and numerical results clarify the role of a single vertical SEAHIVE® unit in scour processes. Flume experiments showed that replacing a circular monopile with a standalone SEAHIVE® monopile does not reduce maximum scour depth; in fact, depending on orientation and base condition, the equilibrium scour depth around the SEAHIVE® can be slightly greater than that around the circular monopile. The numerical simulations extend these findings by demonstrating that internal perforation patterns and their vertical placement significantly influence wake structure and scour distribution: a fully perforated SEAHIVE® produces a more diffused wake and a broader, shallower scour footprint than partially perforated or zigzag layouts. These results suggest that single SEAHIVE® units are best viewed as flow-altering elements whose geometry can be tuned to weaken vortices and redistribute scour, and they provide a necessary foundation for future configurations—such as skirts or upstream groups—rather than as direct one-for-one replacements for conventional monopiles.

GROUP SEAHIVE® SYSTEM

Group SEAHIVE® refers to an arrangement of multiple SEAHIVE® elements placed horizontally in front of a cylindrical monopile, intended to disrupt oncoming flow and reduce local scour formation. Unlike a single SEAHIVE® monopile, which operates based on its own geometry, the group configuration investigates how the spatial placement of SEAHIVE® units at various upstream distances (specifically 2D, 3D, and 4D, where D is the pier diameter) attenuates the strength of downflow and horseshoe vortices around the pier. This experimental and numerical campaign represents a novel approach to evaluating horizontal proactive bed-armoring strategies, particularly for bridge pier applications in flowing water conditions.

Scour Assessment for Group SEAHIVE® System

The group tests used the same flume, sediment, and hydraulic conditions described in the Materials and Methodology Section. The experiments included a 4.0 cm diameter PVC circular monopile as the control, a hydrodynamically equivalent SEAHIVE® monopile, and SEAHIVE® groups installed upstream at spacings of 2D, 3D, and 4D. The equilibrium scour topography was examined for the control monopile, the single SEAHIVE® monopile, and the SEAHIVE® group configurations at 2D, 3D, and 4D spacings. Figure 10 presents the final scoured-bed contours derived from the photogrammetric meshes for each configuration, illustrating how sediment transport responds to the different upstream flow modifications. In the control case (Figure 10a), a wide and relatively deep scour hole forms around the monopile, with asymmetric downstream deposition and lateral scour extending toward the flume walls. The SEAHIVE® monopile (Figure 10b) shows a somewhat reduced and more symmetrical scour region, with less pronounced downstream erosion. In the group configurations (Figures 10c–10e), the SEAHIVE® units substantially moderate sediment disturbance, particularly at 3D and 4D spacings, where the scour hole is shallower and more localized around the pier. At 2D spacing, some flow interference produces additional deposition immediately behind the monopile, whereas at 3D spacing the wake zone appears largely preserved, with only limited scour development near the pier.

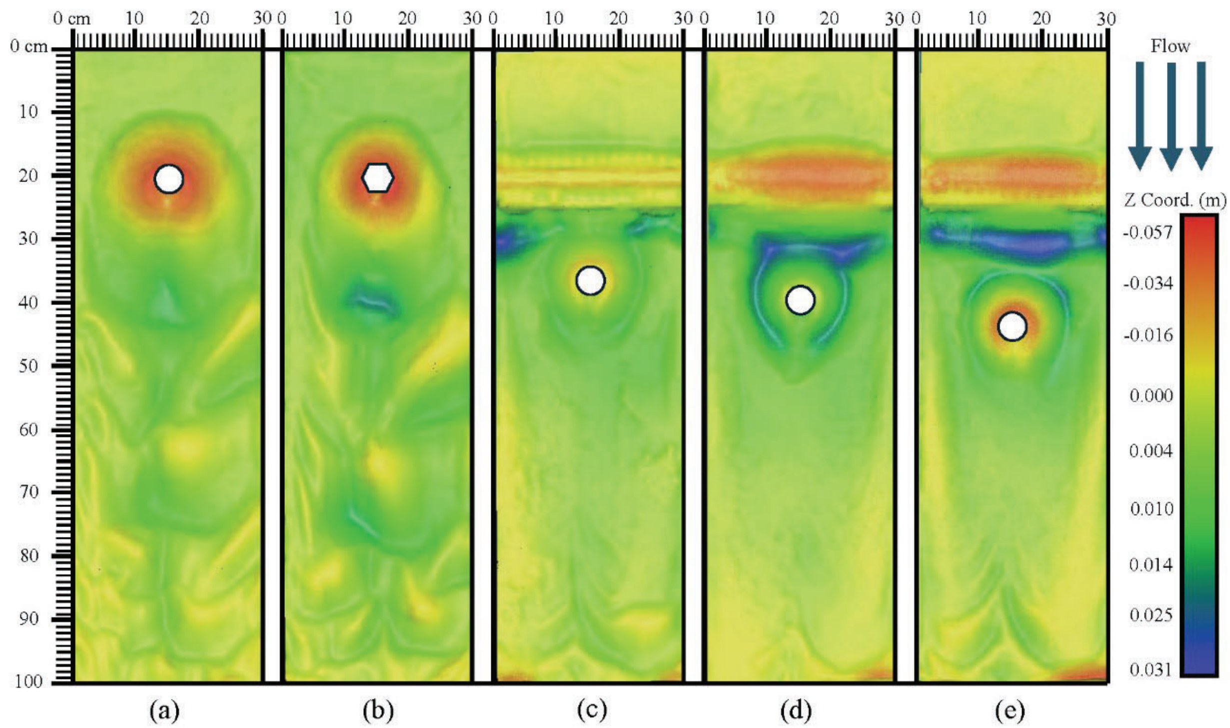

Figure 10. Scoured bed condition at equilibrium state for all cases: a) control case with circular monopile, b) SEAHIVE® monopile, c) SEAHIVE® group at 2D distance, d) SEAHIVE® group at 3D distance, e) SEAHIVE® group at 4D distance.

Figure 11 and Figure 12 highlight the scour profiles for the control case and SEAHIVE® configurations in the longitudinal and transverse directions. The control case displays a deep scour contour in both directions. Notably, the slope angle measured in the experimental contour of the control case matches the friction angle obtained from direct shear tests performed on the loose sand, of 31 degrees, confirming the consistency and accuracy of the experimental results (Tao et al. 2018; Unger and Hager 2007). The transverse and longitudinal cross sections for the SEAHIVE® monopile shown in the upper left panel in Figure 11 and Figure 12 are like the control case, displaying only a slight reduction in both directions.

In the longitudinal direction (Figure 11), the SEAHIVE® group arrangements show a reduced reduction in scour depth compared to the control case, particularly in the downstream wake region (e.g., the region to the right of the monopile) where the scour contours remain shallower and more uniform. Similarly, in the transverse direction (Figure 11), the SEAHIVE®

configurations exhibit less pronounced scour depressions and reduced variability across the sediment bed, demonstrating their capacity to stabilize the surrounding sediment.

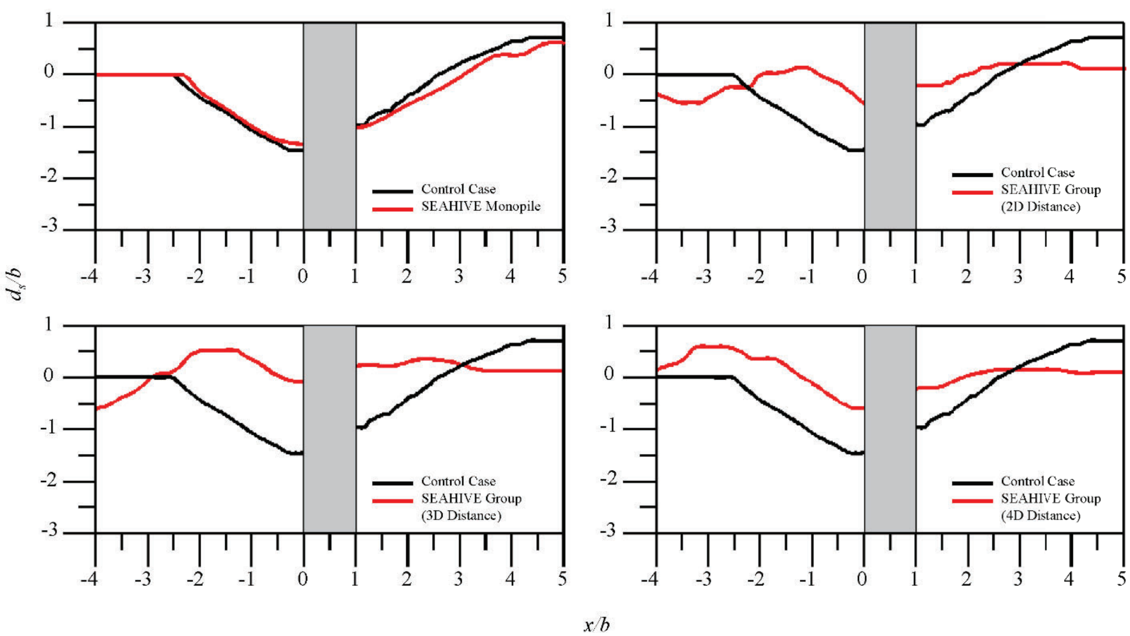

Figure 11. Bed slope condition compared with control case in longitudinal direction.

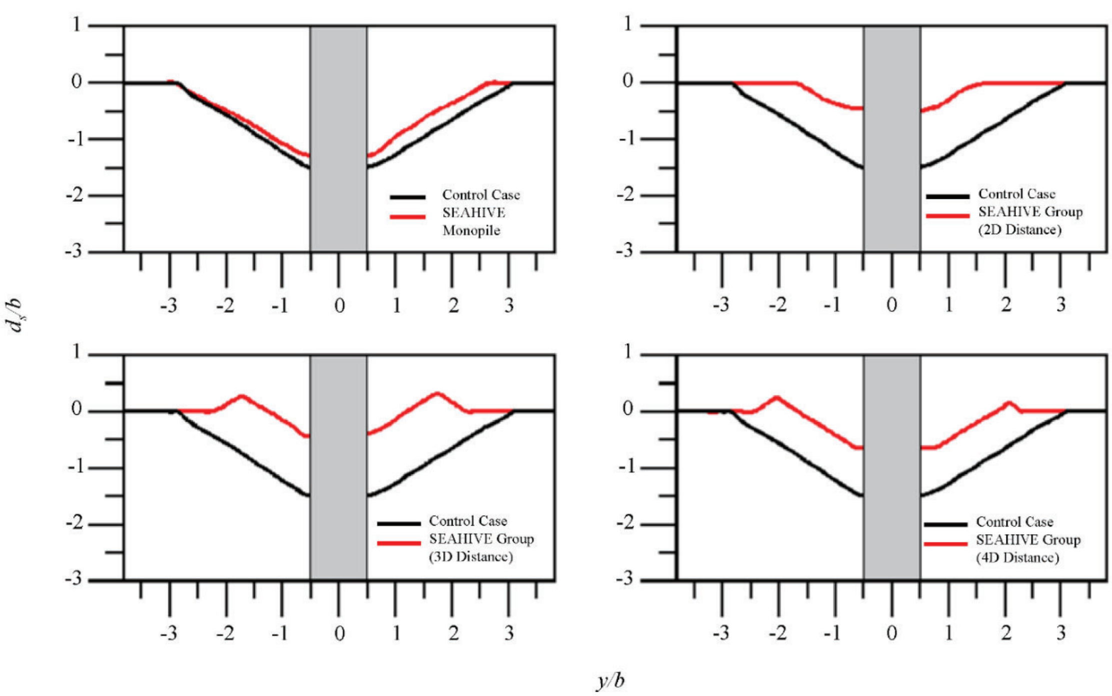

Figure 12. Bed slope condition compared with control case in transverse direction.

The empirical model by Cheng et al. (2016) was used to predict the equilibrium scour depths for all test configurations, and the results were compared to the experimental measurements. Table 2 shows the predicted scour depths (d_{se}) alongside the experimental values for each configuration. The Cheng model demonstrated excellent agreement with the experimental data, with low root mean square errors (RMSE) and high correlation coefficients (R^2) for all configurations. For the circular monopile, the model predicted a scour depth of 5.79 cm, closely matching the measured 5.7 cm. Similarly, for the SEAHIVE® monopile, the predicted scour depth of 5.27 cm was nearly identical to the experimental value of 5.3 cm (RMSE = 0.06, R^2 = 0.999).

Table 2. Experimental validation with Cheng et al. (2016) model.

Experimental Configuration	C value [Cheng]	n value [Cheng]	d_{se} (cm) [Exp.]	d_{se} (cm) [Cheng]	RMSE	R^2
Circular Monopile (D = 4.0 cm)	0.430	0.428	5.70	5.79	0.09	0.997
SEAHIVE ® Monopile ($D_{equiv.}$ = 4.0 cm)	0.583	0.526	5.30	5.27	0.06	0.999
Circular Monopile with SEAHIVE ® Group at 2D Distance	1.887	0.818	1.50	1.54	0.05	0.984
Circular Monopile with SEAHIVE ® Group at 3D Distance	2.100	0.524	1.70	1.72	0.04	0.991
Circular Monopile with SEAHIVE ® Group at 4D Distance	0.230	0.216	2.30	2.52	0.1	0.962

d_{se} is the equilibrium scour depth, RMSE is root mean square error.

The model also closely matched the experimental results for the SEAHIVE® group configurations, with predicted scour depths of 1.54 cm, 1.72 cm, and 2.52 cm for the 2D, 3D, and 4D spacings, respectively, compared to the measured values of 1.5 cm, 1.7 cm, and 2.3 cm. The RMSE values were consistently low (0.05 to 0.10), and the R^2 values were high, confirming the accuracy and reliability of the Cheng et al. (2016) model in predicting scour depths for these experimental setups. Figure 13 shows the experimental data plotted on top of the predicted scour development curve for each configuration, note the experimental data here are the average of the two replicates for each test.

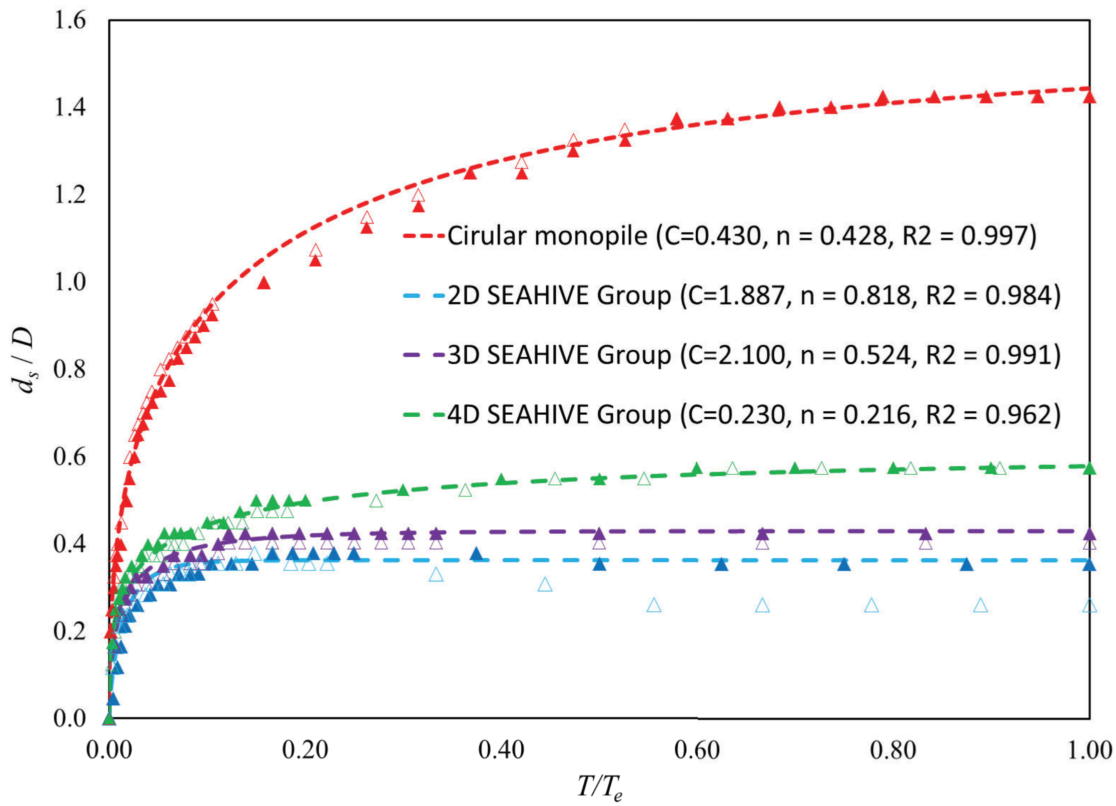

Figure 13. Experimental data plotted against Cheng et al. (2016) model.

The experimental results for the circular monopile reaffirm findings from prior research and existing literature. In the control case, approximately 67% of the total scour depth occurred within the first 60 minutes, aligning with observations by Melville and Chiew (1999). Their study noted that under clear-water conditions, scour depth typically reaches 50% to 80% of the equilibrium depth within the first 10% of the time to equilibrium. The SEAHIVE® monopile behaved similarly, reaching 76% percent of the total scour depth withing the first hour, like Farooq and Ghumman (2019) evaluation of a hexagonal element, which achieved a 78% reduction total scour depth. The scaled SEAHIVE ® monopile, with a hydrodynamic equivalent diameter, exhibited a 7% reduction in scour depth and 22.8% in scour volume when compared to the control case.

To validate that all experiments were conducted under clear-water conditions, the control case was compared to empirical scour models, with the Cheng et al. (2016) model selected for its best fit to the circular monopile data. This model uses two empirical coefficients, C and n, where C relates to sediment interaction and time to reach equilibrium, and n governs the rate of scour development. Since sediment properties were constant across tests, variations in C primarily reflect differences in experimental configurations. Higher n values indicate rapid initial scour, while lower values suggest gradual development. These coefficients enabled direct comparison of scour progression across configurations. The SEAHIVE® monopile showed the lowest percent error against the Cheng et al. (2016) model, supporting its classification under clear-water conditions (Table 3).

Table 3 Percent error between experimental and Cheng model data.

Experimental Configuration	d_s (*cm*) [Exp.]	d_s (*cm*) [Cheng]	Absolute Error	Percent Error (%)
Circular Monopile (D = 4.0 cm)	5.70	5.79	0.09	1.58
SEAHIVE ® Monopile (D_{equiv} = 4.0 cm)	5.30	5.27	0.03	0.57
Circular Monopile with SEAHIVE ® Group at 2D Distance	1.50	1.54	0.04	2.67
Circular Monopile with SEAHIVE ® Group at 3D Distance	1.70	1.72	0.02	1.18
Circular Monopile with SEAHIVE ® Group at 4D Distance	2.30	2.52	0.22	9.57

The SEAHIVE® group at 2D spacing produced the most scour depth reduction but did not maintain classic clear-water conditions, as slight backfilling of the scour hole was observed. This behavior suggests intensified flow interactions immediately upstream of the pier due to proximity of the SEAHIVE® elements. Despite this, the 2D configuration achieved a 77.2% reduction in scour depth and 96.4% reduction in scour volume relative to the control case. The C coefficient for the 2D spacing was approximately 4.4 times greater than the control case, indicating enhanced disruption of scour-generating vortices.

The SEAHIVE® group at 3D spacing demonstrated similar scour volume reduction and maintained clear-water conditions. While the C coefficient remained high, the moderate n exponent suggested a balanced scour progression with effective sediment protection. In contrast, the 4D spacing setup was less effective, as the SEAHIVE® elements were too far upstream to influence the flow near the monopile. Higher n values at 2D spacing reflected rapid initial scour, while lower values at 4D spacing indicated more gradual progression but less protective effect. Intermediate n values at 3D spacing indicated an optimal balance between reduced scour volume and moderated scour progression. Figure 14 displays the percent reduction in scour volume for each SEAHIVE® configuration relative to the control pier. A clear inverse relationship is observed between SEAHIVE ® group spacing and scour volume reduction, affirming that closer placement generally yields better performance in terms of sediment retention and vortex mitigation.

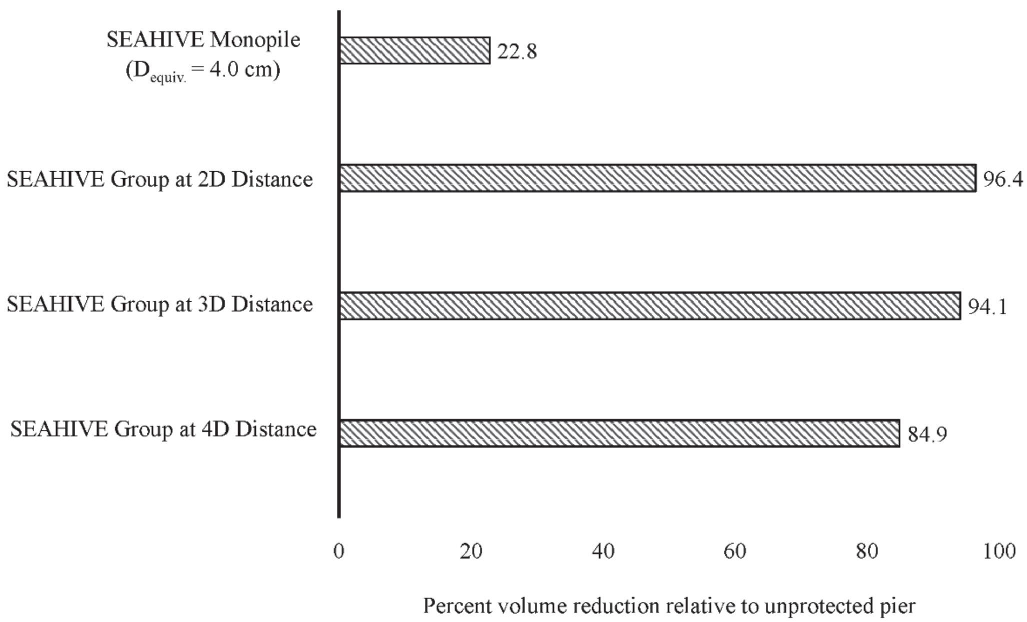

Figure 14. Comparison of equilibrium scour volume for all cases compared to the unprotected pier.

Numerical Investigation of Grouped SEAHIVE ® Configurations

The numerical simulation was conducted to examine hydrodynamic behavior and scour potential around grouped SEAHIVE® arrays installed upstream of a monopile foundation. The two-phase Eulerian model framework, validated by the experimental setup, was used to analyze flow dynamics such as tangential velocity, near-bed velocity magnitude, and internal vector field patterns. Attention was given to the effect of SEAHIVE® spacing on modulating flow energy and suppressing erosive forces. The computational model is first validated by our flume experiments with a 4.00 cm diameter monopile and with a 4.00 cm monopile and SEAHIVE® unit distanced at 3D in front of the monopile (shown in Figure 13).

Figure 15 (a) highlights a rapid erosion phase in front of the monopile during the initial 30 min. At final time step (100 min), the final scour depth is $d_s/D \approx 0.956$. In Figure 15 (b), the 3D SEAHIVE® case similarly shows good agreement between numerical and experimental data, with rapid scour development in the first 20 min followed by a gradual stabilization phase. Ultimately the scour stabilizes to $d_s/D \approx 0.378$. The results from validation tests confirm that our numerical model is accurately tuned and can subsequently be used for detailed analysis of the experimental results.

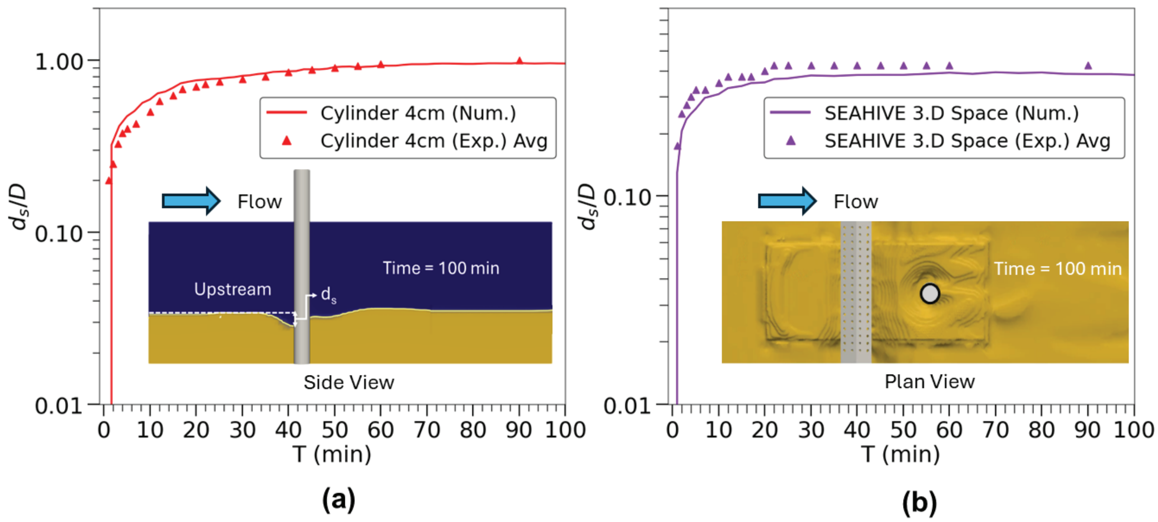

Figure 15 Validation of the numerical model against experimental results: (a) Comparison with our experimental results for D = 4 cm; (b) Comparison with our experimental results for SEAHIVE® 3D Spacing (scaled Y axis for visualization).

Tangential velocity, calculated as $\sqrt{Ux^2+Uz^2}$ where U_x and U_z represent the longitudinal and transverse velocity components respectively, was examined 3 mm above the sediment bed to assess the near-bed stress conditions. Figure 16 shows the tangential velocity fields near the bed surface across different configurations and time steps. In the Control Case (i.e., without SEAHIVE®), the peak tangential velocity near the monopile reached 28.8 cm/s, indicating strong localized shear. When SEAHIVE® groups were introduced, the inner zone velocity around the monopile decreased, most notably in the 2D configuration where the peak value dropped to 19.8 cm/s. In contrast, the 4D configuration exhibited higher velocity concentrations near the cylinder edge, increasing from 25.8 cm/s to 29.1 cm/s, suggesting a weaker flow control due to the wider spacing.

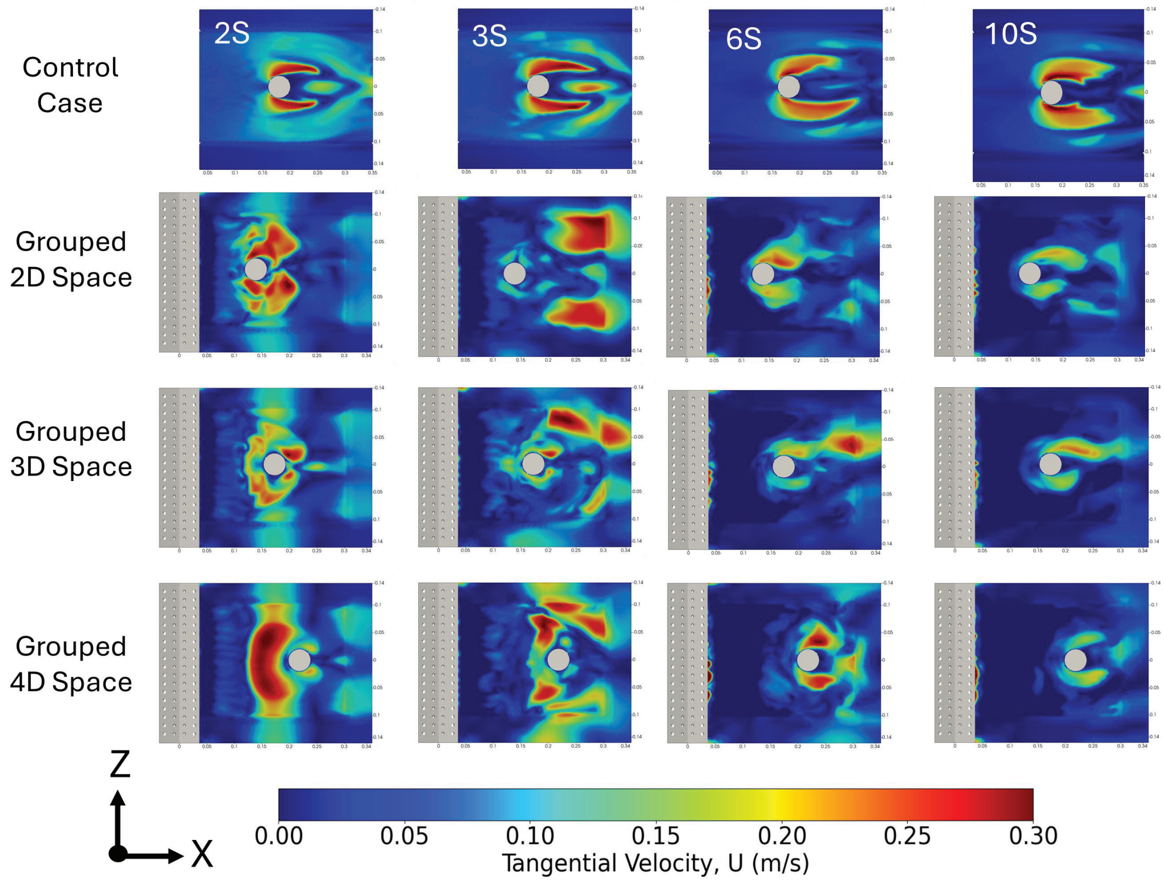

Figure 16. Visualization of tangential velocity near bed surface at different time steps.

Velocity magnitude distributions along the cyclic plane were assessed to understand flow behavior over time (Figure 17). In the Control Case, flow decelerates sharply at the monopile face, forming a low-velocity zone, followed by high-speed recovery and strong shear gradients in the wake. The 2D SEAHIVE® setup disrupts this pattern, creating a broad low-velocity region near the bed and suppressing wake formation, resulting in smoother velocity transitions. The 3D configuration offers moderate disruption, but some flow bypasses the SEAHIVE® group and reattaches near the monopile. In contrast, the 4D setup allows faster reacceleration through wider gaps, increasing bed velocities downstream and reducing shear mitigation.

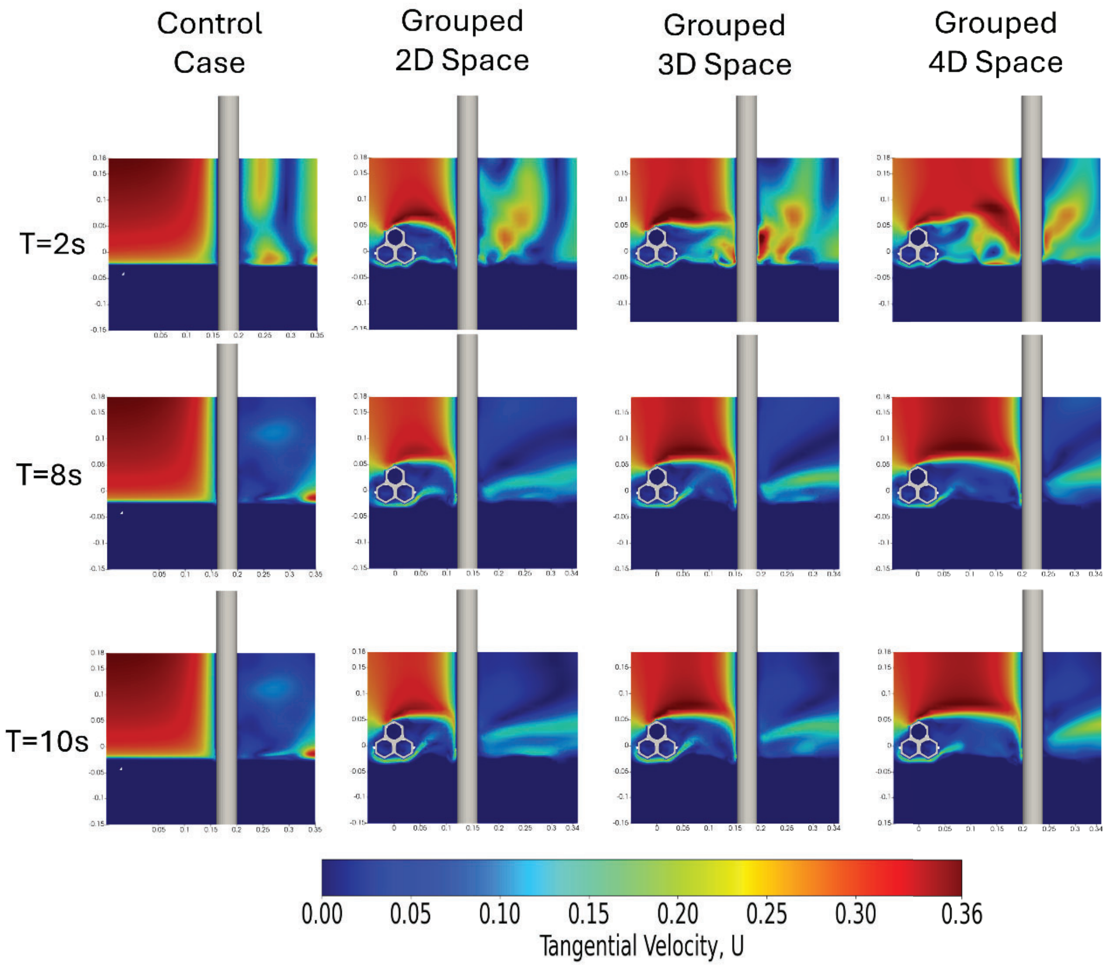

Figure 17. Visualization of velocity magnitude at cyclic plane in longitudinal.

The bed shear stress field offers insight into the interaction between near-bed velocity gradients and sediment stability. The bed shear stress, $\tau = \mu(\nabla.\ U)_{y=3mm}$ is calculated near the bed surface at a height of 3 mm from the sediment surface (Figure 18), where μ is the dynamic viscosity of water and $\nabla.\ U$ is the gradient of the velocity at that surface. In the Control Case, two narrow, high-intensity stress lobes appear directly behind the monopile, with values reaching 0.030 Pa. These lobes remain concentrated in the wake region and elongate with time, indicating persistent vortex shedding and localized scour potential. When the monopile is protected by a SEAHIVE® group, especially in the 2D spacing configuration, the stress field becomes more dispersed and radially symmetric. At step 2s, the peak stress for the 2D spacing reaches only 0.021 Pa, showing a 24% reduction relative to the Control Case. The stress is more evenly distributed around the cylinder, with multiple weaker vortical zones forming instead of a dominant shear core.

In contrast, the 4D configuration displays a stress field that increasingly resembles the Control Case, with values nearing 0.029 Pa and a distinct shear band forming behind the monopile.

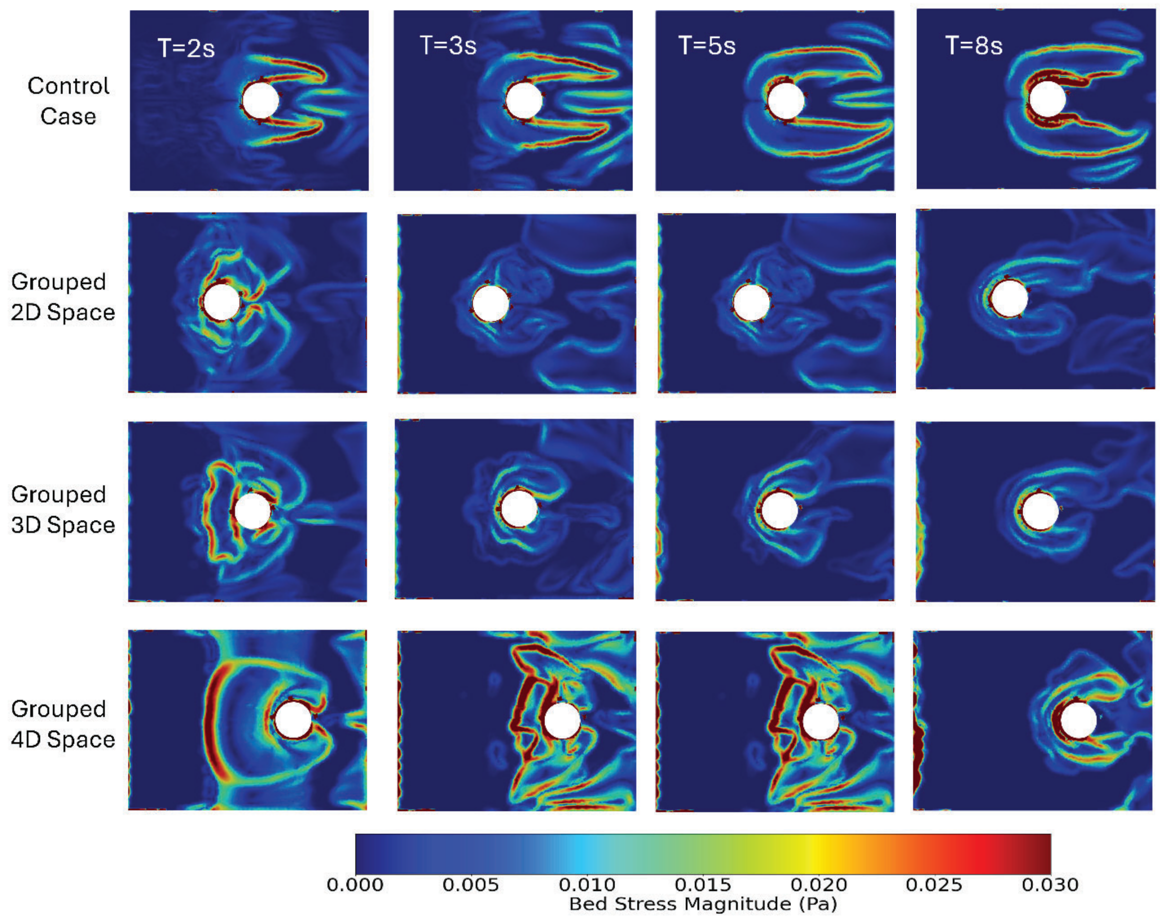

Figure 18. Bed stress magnitude at 3 mm above the sediment surface.

Group SEAHIVE® System Summary

The grouped SEAHIVE experiments and simulations show that tighter upstream placement offers the strongest scour mitigation, with the 2D configuration giving the greatest reduction in scour depth and volume in both physical and computational studies but also departing from classical clear-water conditions. In contrast, the 4D spacing positions the group too far upstream to meaningfully alter near-bed hydraulics at the pier, limiting its effectiveness. Numerical results indicate that a 3D spacing still yields clear reductions in bed shear stress, tangential and vertical velocities, and vortex strength while preserving clear-water conditions, suggesting that 3D offers the most balanced and practical configuration for group SEAHIVE® installations.

While these combined experimental and numerical findings highlight the potential of SEAHIVE® units as an effective, bio-inspired flow-altering countermeasure, several limitations constrain how broadly they can be generalized. Both the flume tests and SedFOAM simulations were conducted at laboratory scale under steady, unidirectional flow, limiting Reynolds number similarity and excluding important field processes such as flood hydrographs, tidal reversals, debris loading, and multi-directional wave–current interaction that are known to influence scour initiation and progression. The narrow flume width restricted the range of feasible configurations to inline, horizontally stacked groups at 2D, 3D, and 4D; attempts to test vertical barriers or skirt-type SEAHIVE® rings around the pier were constrained by stability and side-wall interference, and shorter units or alternative layouts (e.g., staggered, radial, or mixed-height arrays) remain unexplored. In addition, all tests were performed in clean sand beds without biofouling, vegetation, or benthic habitat interactions, whereas in existing coastal SEAHIVE® deployments the units function simultaneously as hydraulic and ecological structures, and such environmental factors may further enhance scour mitigation or alter local hydraulics. Consequently, the present results should be viewed as a first step that demonstrates promising performance and identifies 3D spacing as an optimized configuration in controlled conditions, while underscoring the need for field-scale validation, broader configuration studies, and assessment under realistic, variable hydraulic and environmental regimes.

CONCLUSIONS

This phase of research established and validated a combined experimental–numerical framework to evaluate SEAHIVE® as a proactive scour countermeasure, and demonstrated that SEAHIVE® elements can meaningfully alter near-bed hydraulics and reduce local scour around monopile foundations. Working at laboratory scale, the study first assessed single SEAHIVE® units relative to conventional circular monopiles, showing that while a standalone SEAHIVE® replacement does not universally reduce scour depth in all orientations, the perforated, hexagonal geometry systematically modifies flow structure, vortex development, and sediment transport in ways that can be leveraged in future skirt-type and upstream configurations. Building on this, the grouped SEAHIVE® phase examined horizontally stacked three-unit arrays positioned upstream of the pier and identified that closer placement produces stronger scour mitigation, with the 2D configuration giving the greatest reduction in scour magnitude but no longer behaving as a clear-water scour case, and the 4D configuration being too far upstream to fully suppress high-energy vortices at the pier. The integrated experimental and SedFOAM analyses highlighted the 3D configuration as an especially promising arrangement: it preserves clear-water conditions while substantially reducing bed shear stress, tangential and vertical velocities, and coherent vortex structures near the pier, resulting in a more stable bed and shallower, more localized scour.

Importantly, this work should be viewed as the first phase of a larger SEAHIVE® scour-mitigation program. A key outcome is the development and validation of a high-fidelity, two-phase numerical model that reliably reproduces laboratory scour evolution for control and SEAHIVE® cases, providing a trusted platform to explore additional configurations beyond those physically tested. With a calibrated model and demonstrated benefits for specific geometries and spacings, subsequent research can now systematically investigate a broader design space computationally—including staggered, radial, and mixed-height groupings; skirt rings around monopiles; variable unit length and porosity; and combinations with sacrificial piles or conventional armoring—before down-selecting to the most promising alternatives for testing in larger, more hydraulically representative flumes. At the same time, scaling efforts should target higher Reynolds numbers, variable hydrographs, and compound loading (e.g., waves plus currents, debris, and ice) to better mirror field conditions and to quantify SEAHIVE® performance under extreme events.

To move from proof-of-concept toward engineering practice, several next steps are recommended. First, large-scale flume campaigns and targeted pilot installations at bridge sites or instrumented testbeds should be used to validate numerically optimized configurations under realistic flow, sediment, and structural conditions, and to capture long-term performance, maintenance needs, and interactions with biofouling and habitat development. Second, these data should be synthesized into preliminary design guidelines: for example, recommended SEAHIVE® group spacings and layouts as a function of pier diameter, flow intensity, sediment characteristics, and scour risk level; criteria for selecting single versus grouped units or hybrid systems; and suggested embedment depths and orientations. Third, parametric studies combining the numerical model, flume results, and pilot observations can support cost-benefit analyses that compare SEAHIVE® systems with traditional countermeasures such as riprap, gabions, collars, and sacrificial piles, accounting not only for installation and lifecycle costs but also for co-benefits like habitat creation, reduced maintenance, and resilience under climate-driven extremes. Ultimately, by iterating between computation, laboratory testing, and field pilots, the SEAHIVE® program can deliver engineer-ready design tools (e.g., simplified sizing charts, configuration selection matrices, and integration guidance with existing design codes) and evidence-based economic assessments that enable agencies and practitioners to confidently incorporate SEAHIVE® and similar bio-inspired systems into bridge scour mitigation portfolios.

DATA AVAILABILITY STATEMENT

All experimental data and computational information that support the findings of this study are in the Zenodo Data Share repository with the identifier https://zenodo.org/records/18175863.

REFERENCES

Arneson, L. A., L. W. Zevenbergen, P. F. Lagasse, P. E. Clopper, and Ayres Associates. 2012. Evaluating Scour at Bridges: Fifth Edition.

Bergmann, H., and H. Oumeraci. 2012. "Wave Loads on Perforated Caisson Breakwaters." *Coastal Engineering*, 1622–1635. American Society of Civil Engineers. https://doi.org/10.1061/40549(276)126.

Bestawy, A., T. Eltahawy, A. Alsaluli, A. Almaliki, and M. Alqurashi. 2020. "Reduction of local scour around a bridge pier by using different shapes of pier slots and collars." *Water Supply*, 20 (3): 1006–1015. https://doi.org/10.2166/ws.2020.022.

Bharadwaj, M. R., L. K. Gupta, M. Pandey, and M. Valyrakis. 2025. "Countermeasures for local scour around the bridge pier: a review." *Acta Geophys*., 73 (1): 701–728. https://doi.org/10.1007/s11600-024-01361-z.

Breusers, H. N. C., G. Nicollet, and H. W. Shen. 1977. "Local Scour Around Cylindrical Piers." *Journal of Hydraulic Research*, 15 (3): 211–252. https://doi.org/10.1080/00221687709499645.

Castillo, R., S. Kulesza, and L. Rhode-Barbarigos. 2025. "Experimental Investigation for a Novel Bio-Inspired Scour Countermeasure." Proceedings of Geo-Congress 2025, 463–473. https://doi.org/10.1061/9780784485996.044.

Chauchat, J., Z. Cheng, T. Nagel, C. Bonamy, and T.-J. Hsu. 2017. "SedFoam-2.0: a 3-D two-phase flow numerical model for sediment transport." *Geoscientific Model Development*, 10 (12): 4367–4392. https://doi.org/10.5194/gmd-10-4367-2017.

Cheng, N. S., Y. M. Chiew, and X. Chen. 2016. "Scaling Analysis of Pier-Scouring Processes." *Journal of Engineering Mechanics*, 142 (8): 06016005. https://doi.org/10.1061/(ASCE)EM.1943-7889.0001107.

Craswell, T., and S. Akib. 2020. "Reducing Bridge Pier Scour Using Gabion Mattresses Filled with Recycled and Alternative Materials." *Eng*, 1 (2): 188–210. https://doi.org/10.3390/eng1020013.

Egan, P., R. Sinko, P. R. LeDuc, and S. Keten. 2015. "The role of mechanics in biological and bio-inspired systems." *Nat Commun*, 6 (1): 7418. https://doi.org/10.1038/ncomms8418.

Farooq, R., and A. R. Ghumman. 2019. "Impact Assessment of Pier Shape and Modifications on Scouring around Bridge Pier." *Water*, 11 (9): 1761. https://doi.org/10.3390/w11091761.

Faroughi, S. A. and Huber, C. (2015). "A generalized equation for rheology of emulsions and suspensions of deformable particles subjected to simple shear at low Reynolds number." *Rheologica Acta*, 54, 85–108.

Faroughi, S. and Huber, C. (2016). "A theoretical hydrodynamic modification on the soil texture analyses obtained from the hydrometer test." *Géotechnique*, 66(5), 378–385.

Feld, J., and K. L. Carper. 1996. *Construction Failure*. John Wiley & Sons.

Fugazza, M., and L. Natale. 1992. "Hydraulic Design of Perforated Breakwaters." *Journal of Waterway, Port, Coastal, and Ocean Engineering*, 118 (1): 1–14. https://doi.org/10.1061/(ASCE)0733-950X(1992)118:1(1).

Harris, J. M., R. J. S. Whitehouse, N. S. Tavouktsoglou, and P. M. Godinho. 2019. "Foundation Scour as a Geohazard." *Journal of Waterway, Port, Coastal, and Ocean Engineering*, 145 (6): 04019022. https://doi.org/10.1061/(ASCE)WW.1943-5460.0000523.

Lagasse, P. F., Zevenbergen, L. W., Spitz, W. J., & Arneson, L. A. (2012). *Stream stability at highway structures* (4th ed.; Hydraulic Engineering Circular No. 20, FHWA-HIF-12-004). Federal Highway Administration.fhwa.dot

Melville, B. W. 1997. "Pier and Abutment Scour: Integrated Approach." *Journal of Hydraulic Engineering*, 123 (2): 125–136. https://doi.org/10.1061/(ASCE)0733-9429(1997)123:2(125).

Melville, B. W., and Y.-M. Chiew. 1999. "Time Scale for Local Scour at Bridge Piers." *Journal of Hydraulic Engineering*, 125 (1): 59–65. https://doi.org/10.1061/(ASCE)0733-9429(1999)125:1(59).

Melville, B. W., and Coleman, S. E. (2000). *Bridge scour*. Water Resources Publications.

Melville, B. W., and A. J. Sutherland. 1988. "Design Method for Local Scour at Bridge Piers." *Journal of Hydraulic Engineering*, 114 (10): 1210–1226. https://doi.org/10.1061/(ASCE)0733-9429(1988)114:10(1210).

Raudkivi, A. J., and R. Ettema. 1983. "Clear - Water Scour at Cylindrical Piers." *Journal of Hydraulic Engineering*, 109 (3): 338 - 350.

https://doi.org/10.1061/(ASCE)0733-9429(1983)109:3(338).

Richardson, E. V., S. R. Davis, National Highway Institute (U.S.), and United States. Federal Highway Administration. Office of Bridge Technology. 2001. Evaluating Scour at Bridges [Fourth Edition].

Roulund, A., B. Sumer, J. Fredsoe, and J. MICHELSEN. 2005. “Numerical and experimental investigation of flow and scour around a circular pile.” *Journal of Fluid Mechanics*, 534: 351–401. https://doi.org/10.1017/S0022112005004507.

Schoonees, T., A. Gijón Mancheño, B. Scheres, T. J. Bouma, R. Silva, T. Schlurmann, and H. Schüttrumpf. 2019. “Hard Structures for Coastal Protection, Towards Greener Designs.” *Estuaries and Coasts*, 42 (7): 1709–1729. https://doi.org/10.1007/s12237-019-00551-z.

Schuring, J. R., R. Dresnack, E. Golub, M. A. Khan, M. R. Young, R. Dunne, and N. Aboobaker. 2012. “Review of Bridge Scour Practice in the U.S.” *Scour and Erosion,* 1110–1119. https://doi.org/10.1061/41147(392)112.

Singh, N. B., T. T. Devi, and B. Kumar. 2022. “The local scour around bridge piers—a review of remedial techniques.” *ISH Journal of Hydraulic Engineering*, 28 (sup1): 527–540. https://doi.org/10.1080/09715010.2020.1752830.

Tafarojnoruz, A., R. Gaudio, and F. Calomino. 2012. “Evaluation of Flow-Altering Countermeasures against Bridge Pier Scour.” *Journal of Hydraulic Engineering*, 138 (3): 297–305. https://doi.org/10.1061/(ASCE)HY.1943-7900.0000512.

Tao, J., J. Li, X. Wang, and R. Bao. 2018. “Nature-Inspired Bridge Scour Countermeasures: Streamlining and Biocementation.” *Journal of Testing and Evaluation*, 46: 20170517. https://doi.org/10.1520/JTE20170517.

Unger, J., and W. H. Hager. 2007. “Down-flow and horseshoe vortex characteristics of sediment embedded bridge piers.” *Exp Fluids*, 42 (1): 1–19. https://doi.org/10.1007/s00348-006-0209-7.

Wilcox, D. C. 2008. “Formulation of the k-w Turbulence Model Revisited.” *AIAA Journal*, 46 (11): 2823–2838. https://doi.org/10.2514/1.36541.

Xiong, W., C. Cai, R. Zhang, H. Shi, and C. Xu. 2023. “Review of Hydraulic Bridge Failures: Historical Statistic Analysis, Failure Modes, and Prediction Methods.” *Journal of Bridge Engineering*, 28: 03123001. https://doi.org/10.1061/JBENF2.BEENG-5763.

APPENDIX A – DETAILED NUMERICAL MODELING APPROACH

This appendix summarizes the full two-phase mathematical modeling, rheological closures, and vortex-identification procedures used in the SedFOAM simulations. Readers interested in implementation details can refer to the cited literature for complete derivations; the main text focuses on the numerical setup, validation, and key output metrics.

A.1 Two-Phase Governing Equations

The SedFOAM model adopts an Eulerian–Eulerian two-phase formulation following Chauchat et al. (2017), in which both water and sediment occupy each computational cell. Mass conservation for the solid and liquid phases is written as

$$\frac{\partial \phi_s}{\partial t} + \nabla \cdot (\phi_s \mathbf{u}_s) = 0, \tag{A.1}$$

$$\frac{\partial \phi_l}{\partial t} + \nabla \cdot (\phi_l \mathbf{u}_l) = 0, \tag{A.2}$$

where ϕ_s and ϕ_l are solid and fluid volume fractions, and $\mathbf{u}_s$ and $\mathbf{u}_l$ are their velocity vectors. Momentum equations for each phase include pressure gradients, viscous and granular stresses, gravity, and interphase drag coupling:

$$\frac{\partial (\phi_s \mathbf{u}_s)}{\partial t} + \nabla \cdot (\phi_s \mathbf{u}_s \mathbf{u}_s) = -\phi_s \nabla p + \nabla \cdot \boldsymbol{\sigma}_s + \phi_s \rho_s \mathbf{g} + \mathbf{f} - K(\mathbf{u}_s - \mathbf{u}_l) \tag{A.3}$$

$$\frac{\partial (\phi_l \mathbf{u}_l)}{\partial t} + \nabla \cdot (\phi_l \mathbf{u}_l \mathbf{u}_l) = -\phi_l \nabla p + \nabla \cdot \boldsymbol{\sigma}_l + \phi_l \rho_l \mathbf{g} - K(\mathbf{u}_l - \mathbf{u}_s) \tag{A.4}$$

where p is pressure, $\boldsymbol{\sigma}_s$ and $\boldsymbol{\sigma}_l$ are solid and fluid stress tensors, ρ_s and ρ_l are densities, $\mathbf{g}$ is gravitational acceleration, $\mathbf{f}$ represents external forcing, and K is a drag parameter. The drag coefficient K is calculated from particulate Reynolds number and effective particle diameter, incorporating a hindrance function that accounts for increased drag at higher particle concentrations. Detailed expressions follow Schiller-type drag laws and Faroughi and Huber (2015, 2016).

A.2 Fluid-Phase Stresses and Turbulence Closure

Fluid stresses consist of grain-scale viscous stress and Reynolds stress. The total fluid stress tensor $\boldsymbol{\sigma}_l$ is expressed as

$$\boldsymbol{\sigma}_l = 2\mu_{\text{eff},l}\mathbf{S}_l - \frac{2}{3}\rho_l k\mathbf{I}, \tag{A.5}$$

where $\mu_{\text{eff},l} = \mu_{\text{mix}} + \mu_t$ is the effective viscosity combining mixture viscosity and eddy viscosity, $\mathbf{S}_l$ is the deviatoric strain-rate tensor, k is turbulent kinetic energy, and $\mathbf{I}$ is the identity tensor. Eddy viscosity μ_t is computed using the k–ω 2006 turbulence model (Wilcox 2008), which modifies cross-diffusion terms to improve prediction of boundary-layer flows with strong adverse pressure gradients, such as near vertical cylinders. Two-phase k–ω formulations from Chauchat et al. (2017) are used to account for sediment effects on turbulence production and dissipation.

A.3 Solid-Phase Stresses and Granular Rheology

Solid-phase stresses include normal and shear contributions arising from collisions and enduring contacts. Normal stress is decomposed into collisional and permanent-contact components, with maximum packing concentration and frictional transition concentration chosen based on spherical particle properties. Shear stress in the sediment phase is modeled using a blend of kinetic theory of granular flows, appropriate for moderately dense regimes, and dense granular flow rheology (μ(I) rheology) for near-bed, quasi-static conditions. In the μ(I) framework, shear stress is related to pressure through a dynamic friction coefficient that depends on an inertial number I. This blended approach allows the model to represent both mobile and quasi-static sediment layers while maintaining numerical stability.

A.4 Numerical Domain, Boundary Conditions, and Validation

The computational domain is constructed as a rectangular prism measuring 100 cm (X-direction), 33 cm (Y-direction), and 30 cm (Z-direction). It comprises a 20.5 cm deep water column over an underlying sediment bed with median grain size consistent with the experimental Ottawa sand used in the flume. A monopile is centered within the domain to reproduce the experimental test section, and an inflow velocity of 19.4 cm/s is imposed to match the laboratory conditions.

The inlet velocity follows a logarithmic distribution to represent an equilibrium open-channel approach flow.

Boundary conditions are defined to reflect the physical flume setup, including inflow velocities, sediment supply, and outflow behavior:

- **Inlet and outlet boundaries:** At the inlet, fixed-value boundary conditions are applied to velocity and turbulence fields based on equilibrium profiles obtained from uniform-channel flow calculations. For pressure fields p_a and p_r^{bgh}, a zero-gradient (Neumann) condition is used. At the outlet, zero-gradient conditions ($\partial / \partial n = 0$) are specified for all quantities except the reduced pressure p^*, for which a homogeneous Dirichlet boundary condition $p^* = 0$ is imposed. A homogeneous Dirichlet condition is also applied to the kinematic viscosity νat the outlet.

- **Top and bottom boundaries:** At the top, a symmetry-plane boundary is applied to represent the free surface and ensure flow continuity; top boundary conditions for all parameters and velocity components are Neumann-type. At the bottom, a no-slip boundary is imposed for the three velocity components, and a small value is prescribed for turbulent kinetic energy (TKE). Classical wall functions from OpenFOAM are used at the rigid bottom to model near-wall turbulence behavior.

- **Lateral boundaries:** At the lateral sides (front and back), cyclic (periodic) boundary conditions are applied to minimize sidewall effects and emulate a wider flume environment.

- **Cylinder surface boundary:** The monopile (cylinder) surface is represented as a wall boundary, enforcing no-slip conditions and appropriate wall functions for turbulence quantities.

The numerical domain is discretized using an unstructured mesh with refined elements near the SEAHIVE® structure and sediment–water interface to accurately resolve flow separation, turbulence generation, and sediment dynamics. The mesh shown in Figure A. 1 is approximately 2.6 times finer around the cylinder and at the initial interface position compared to the coarser regions of the domain, and the refined region is axisymmetric about the cylinder. For the water column, the mesh is divided into 23 vertical levels, while the sand layer is discretized using 10 vertical levels. Three mesh resolutions—coarse, medium, and fine—were considered in the sensitivity analysis. The medium-resolution mesh consists of approximately 1.73 million cells, while the coarse and fine meshes contain about 0.87 million and 3.0 million cells, respectively. The refined near-bed and near-cylinder discretization is designed to capture steep gradients in velocity and sediment concentration without incurring excessive computational cost.

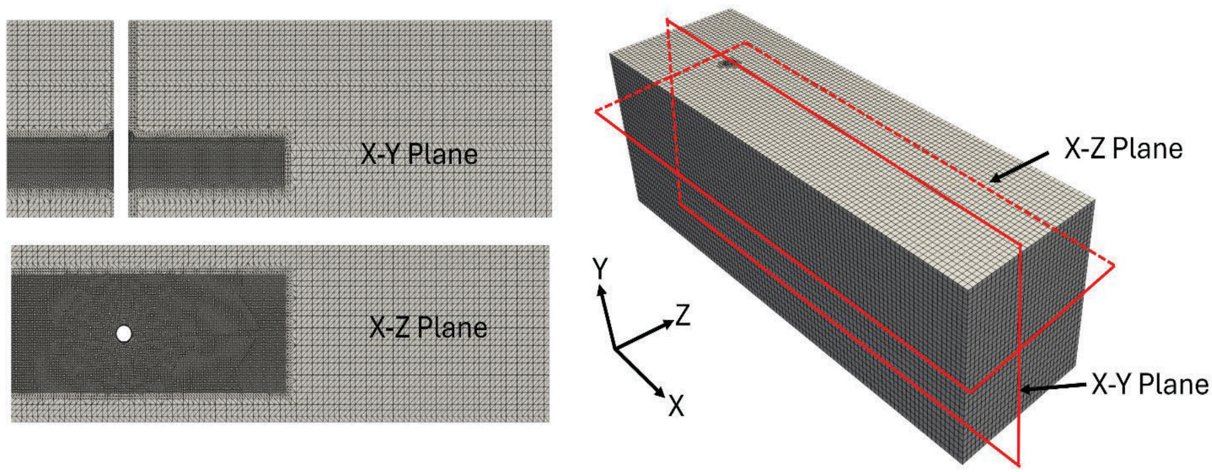

Figure A. 1. Mesh resolution of numerical model.

The numerical model for local scour around a monopile was first validated against the experimental data from Roulund et al. (2005) for a monopile with diameter $D = 10$ cm. The numerical domain was divided into initial water and sediment regions matching the experimental configuration. In this validation, the SedFOAM model used a mesh resolution of 1.73 million cells, whereas Roulund employed meshes of approximately 0.97 million cells. Despite minor differences in boundary conditions and mesh design, the comparisons provided meaningful insight into model performance. The numerical setup included a monopile with diameter $D = 10$ cm, sediment median particle size $d_{50} = 0.26$mm, bulk flow velocity $U = 46$cm/s, and water depth $h = 40$cm. The SedFOAM model was run for 60 min of simulated time.

Figure A. 2 shows the evolution of normalized scour depth d_s/D over time. The numerical results exhibit a rapid increase in scour depth during the initial phase, followed by stabilization after approximately 40 min, consistent with expected scour behavior around a monopile. Experimental data (blue triangles) reach a peak d_s/D of about 1.03 at 30 min, close to the SedFOAM prediction of 1.02. For the case with smaller mesh size, the numerical scour depth slightly overpredicts the experimental values by about 10–15% at later times, whereas the largergrid case shows closer agreement, with differences reduced to approximately 3–5%. At 60 min, SedFOAM predicts a maximum $d_s/D$of 1.11 compared to 1.15 reported by Roulund, indicating that the model is well-calibrated for this benchmark.

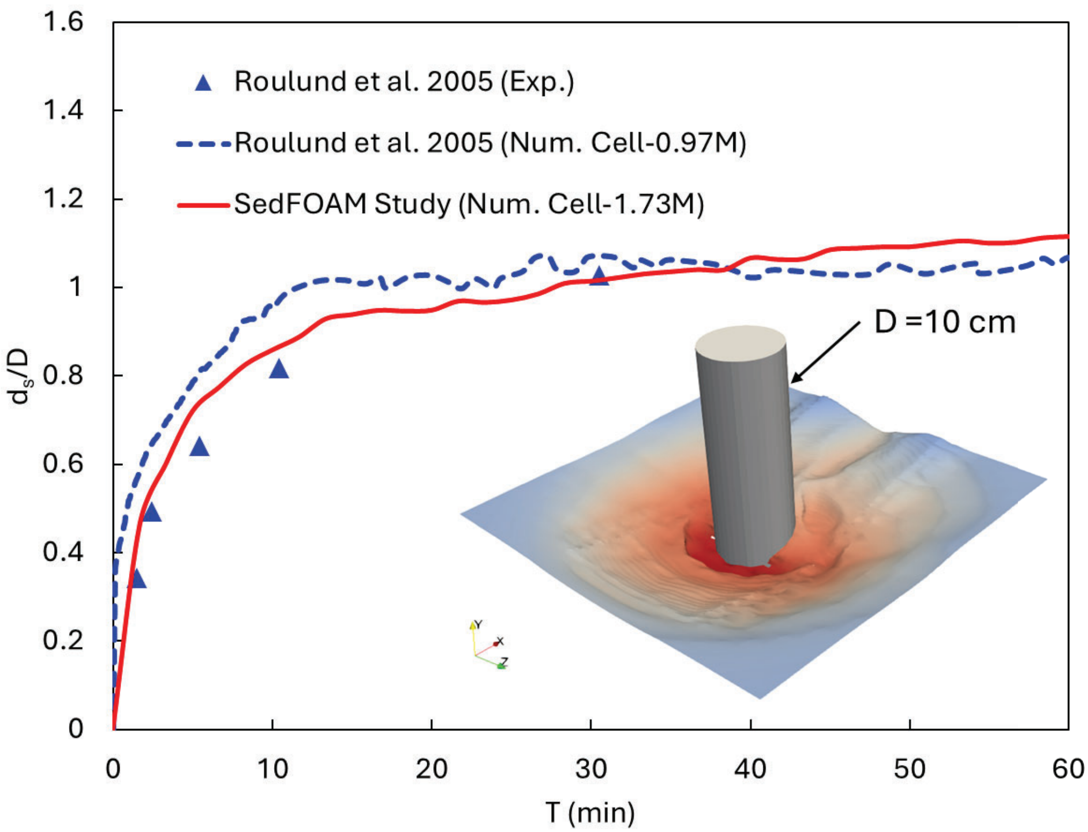

Figure A. 2 Validation of SedFOAM model against Roulund et al. (2005) for D = 10 cm.

Subsequent simulations reproduce the TXST flume setup with a 2.7 cm diameter monopile used in experimental studies of local scour (Castillo et al. 2025). This configuration serves as the Control Case for comparing scour response with SEAHIVE® installations. The finite volume method (FVM) was used to solve the governing equations, and a first-order Euler scheme was employed for time discretization. Simulations were executed in parallel on a high-performance computing cluster; total wall-clock time was approximately 119 hours (4.96 days), with execution time around 427,606 s. Key geotechnical and hydraulic parameters for the present numerical study and the corresponding experimental study are summarized in Table A. 1.

Table A. 1. Summary of geometrical parameters used in these studies.

Variable	Present Study	Experimental Study (Castillo et al. 2025)
Saturated Sand Density ρ_{sat} (g/cm^3)	2.020	2.020
Volume Fraction, $\Phi = \frac{1}{1+e}$	0.618	0.613
Void ratio, $e = \frac{1-\Phi}{\Phi}$	0.617	0.632
Porosity, $n = \frac{e}{1+e}$	0.382	0.387
Critical Shear Velocity, U^* (cm/s)	1.3	1.3
Friction velocity U_f (cm/s)	2.0	-
ReD, δ = V δ / υ	4.0×10^4	4.0×10^4
ReD,υ= VD/ υ	5.2 × 103	5.2 × 103
Froude Number, Fr $\frac{V}{\sqrt{gh}}$	0.137	-
Sheilds Parameter, θ $\frac{u_f^2}{(s-1)\ gD}$	0.46	-
k_s = 2.5 d50 (mm)	0.525	-

After establishing boundary conditions and model parameters, the numerical simulation was run for more than 100 min of simulated time. The corresponding experimental tests were conducted for up to 8 hours, with two independent runs averaged for comparison. Experimental results showed negligible changes in maximum scour depth after about 5 hours, with variations less than 1 mm over 3 hours, satisfying equilibrium conditions. Figure A. 3(a) shows the time evolution of d_s/D for the control monopile case. The numerical scour depth increases rapidly during the initial phase (up to ~20 min), accounting for approximately 85% of the equilibrium scour depth, then slows as sediment transport stabilizes. By around 60–90 min, the numerical scour depth approaches $d_s/D \approx 1.01$, consistent with the experimental equilibrium value. Figure A. 3(b) compares d_s/D evolution for coarse (0.87M cells), medium (1.73M cells), and fine (3.0M cells) mesh resolutions. The coarse mesh underpredicts initial scour depth, whereas the medium and fine meshes produce nearly identical scour evolution and equilibrium values. These results confirm that the medium-resolution mesh provides an optimal balance between accuracy and computational cost.

CREATE

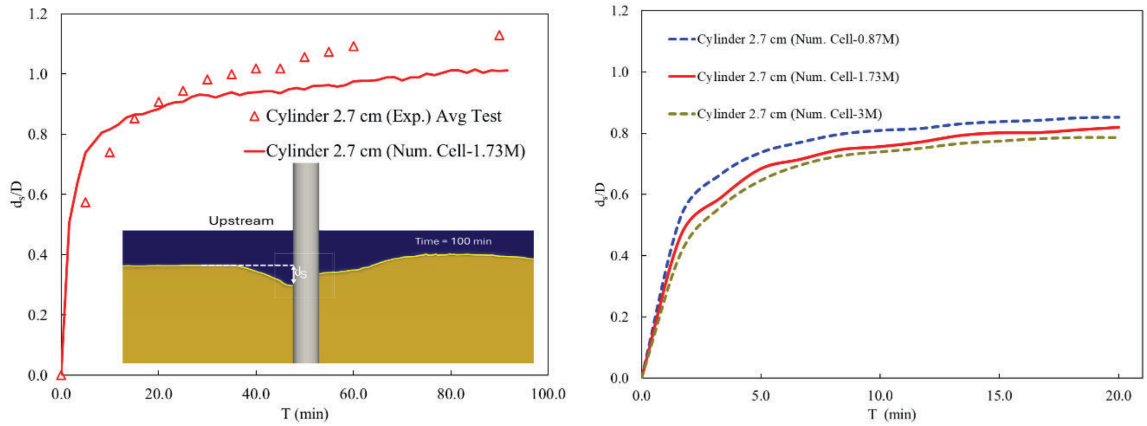

(a) (b)

Figure A. 3. Comparison of scour depth (d_s/D) over time with experimental results for D = 2.7 cm and (b) Scour Depth development for different mesh resolutions upstream.

To further analyze the flow behavior around the monopile, streamline patterns in horizontal planes near the bed (e.g., $y = 10$cm) and at mid-depth were examined as shown in Figure A. 4. These plots illustrate the development of flow separation and vortex shedding in the wake of the cylinder. At early times, the flow around the cylinder is relatively smooth and laminar, with small recirculation zones behind the monopile. As time progresses (e.g., $t \approx 2$s), vortex shedding becomes more pronounced, with larger recirculation zones forming downstream and stronger shear layers developing at the sides. By later stages (e.g., $t \approx 3$–4s), the flow transitions to a fully turbulent regime, characterized by large vortices and an expanded wake region. These patterns illustrate the development of periodic shedding and recirculation, which are closely linked to local scour formation and are further quantified using the Q-criterion and near-bed velocity metrics described in Section A4.

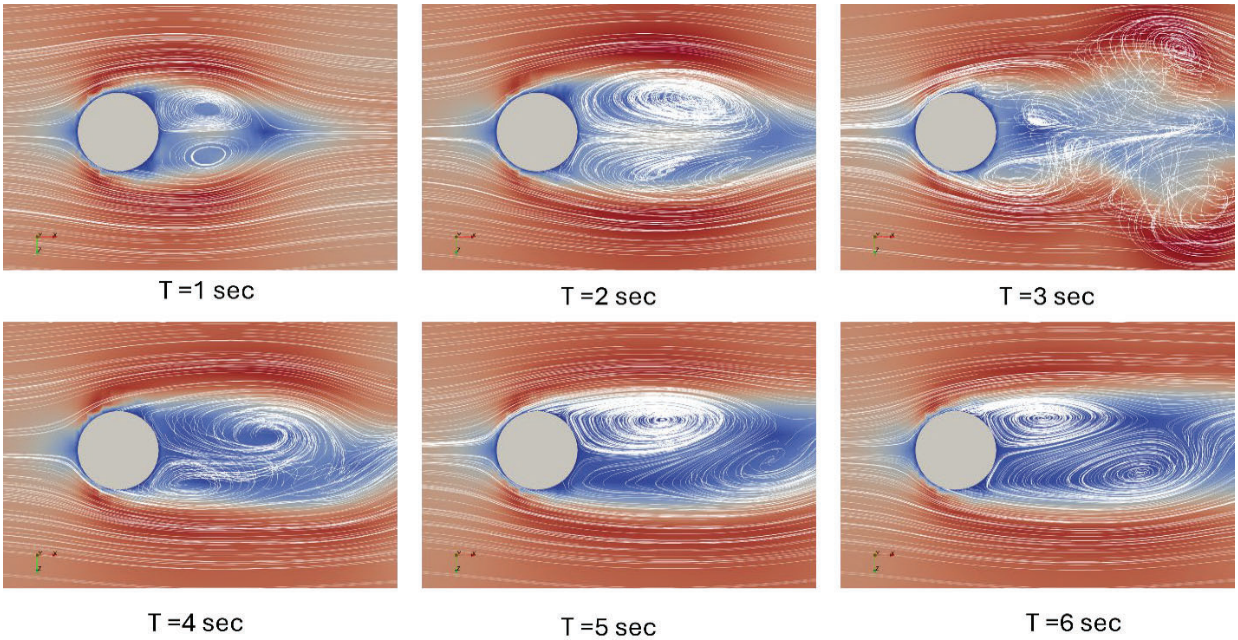

Figure A. 4. Mean flow streamlines on horizontal planes over time stages.

Link to SEAHIVE® Configuration Analyses

The numerical domain, boundary conditions, mesh strategy, and validation results presented in Appendix A.4 establish the reliability of the SedFOAM framework for simulating local scour around cylindrical monopiles under clear-water conditions. These validated settings—together with the governing equations, rheological closures, and flow metrics described in Appendix A1 through Appendix A4—are directly applied in subsequent simulations of single-unit SEAHIVE® monopiles and three-unit SEAHIVE® groups installed upstream of a monopile. For the SEAHIVE® cases, the same domain dimensions, inlet velocity profile, sediment properties, and mesh refinement approach are used, with only the near-pile geometry modified to represent the SEAHIVE® unit or group. As a result, differences in scour depth, scour volume, near-bed velocity, and vortex structure between the control monopile and SEAHIVE® configurations can be attributed to changes in local hydraulics induced by the SEAHIVE® geometry rather than to variations in numerical setup. The results and interpretation of these SEAHIVE® simulations are presented in the main sections of this report.